Heterostructured NiO/IrO$_2$ synergistic pair as durable trifunctional electrocatalysts towards water splitting and rechargeable zinc-air batteries: An experimental and theoretical study

S.C. Karthikeyan [a], Saleem Sidra [a], Shanmugam Ramakrishnan [a,b], Do Hwan Kim [a,c,*], Prince JJ Sagayaraj [d], Karthikeyan Sekar [d], Dong Jin Yoo [a,e,*]

[a] *Department of Energy Storage/Conversion Engineering (BK21 FOUR) for Graduate School, Hydrogen and Fuel Cell Research Center, Jeonbuk National University, Jeonju, Jeollabuk-do 54896, the Republic of Korea*
[b] *School of Engineering, Newcastle University, NE17RU, United Kingdom*
[c] *Division of Science Education, Jeonbuk National University, Jeonju, Jeonbuk 54896, the Republic of Korea*
[d] *Sustainable Energy and Environmental Research Laboratory, Department of Chemistry, Faculty of Engineering and Technology, SRM Institute of Science and Technology, Kattankulathur, Tamil Nadu 603203, India*
[e] *Department of Life Science, Jeonbuk National University, Jeonju, Jeollabuk-do 54896, the Republic of Korea*

ARTICLE INFO

ABSTRACT

Constructing an ultra-durable trifunctional electrocatalyst with high efficiency for HER, OER and ORR has become critical for demanding water splitting and zinc air battery applications. Herein, we demonstrated a rational and efficient strategy to develop a porous nano foam like heterostructured NiO/IrO$_2$ nano foam like electrocatalyst via a facile solvothermal and calcination approach. Experiments revealed that NiO/IrO$_2$-NF shows outstanding HER (η_{10}=42 mV), OER (η_{10}=240 mV), and ORR ($E_{1/2}$=0.80 V) performances with lower over-potentials than many reported trifunctional electrocatalysts. Theoretical investigations on reaction mechanism of NiO/IrO$_2$-NF, S-IrO$_2$ and S-NiO were carried out using density functional theory calculations. The fabricated water electrolyzer required minimum cell voltage of 1.51 V to reach 10 mA cm^{-2} current density with outstanding durability of 600 h and insignificant potential loss. Rechargeable zinc air battery with NiO/IrO$_2$-NF air cathode displays a power density of 134.8 mW cm^{-2} with excellent durability of 100/80/40 h at 2/5/10 mA cm^{-2}.

1. Introduction

Rapid growth in global energy demand and environmental impacts have made researchers focus on sustainable and clean energy solutions [1]. Various renewable energy devices like metal-air batteries, fuel cells, solar cells, and water splitting are in the limelight due to their higher efficiency output for practical applications [2–4]. Among them, water splitting and zinc-air batteries have attracted better attention because of their high energy density, natural abundance of raw materials (i.e., zinc and water), and high safety (using aqueous electrolyte) [5,6]. The oxygen reduction reaction (ORR) and oxygen evolution reaction (OER) are key electrochemical reactions involved in the charge and discharge of rechargeable zinc-air batteries. Similarly, the HER (hydrogen evolution reaction) and OER are the two half-cell reactions for water splitting.

However, the overpotentials required to drive these reactions are higher due to the involvement of multi-step electron transfer and sluggish re-action kinetics. Multiple studies are focused on developing efficient electrocatalysts like Pt-based alloys for HER, Ir/Ru-based alloys for OER and Pt/Pd-based materials for ORR [7–9]. These catalysts are employed in enhancing particular reactions (OER/HER/ORR) based on their in-teractions and electrocatalytic active sites. Moreover, commercial cat-alysts do not provide this trifunctional electrocatalytic activity. Thus, the development of a trifunctional electrocatalyst without limiting its catalytic efficiency remains a crucial task. Development of such multi-functional electrocatalysts reduces the risk of cross contamination, simplifies device fabrication and reduces the overall cost.

Several transition metal-based oxides [10,11], selenides [12], sul-fides [13], tellurides [14], phosphides [15] and their alloys have been

examined for efficient electrocatalysts towards water splitting and zinc-air batteries. Notably, the oxide based electrocatalysts are thermodynamically more stable under prolonged oxidative potentials than their counterpart anions (O>S>N>P) [16]. Thus, oxide-based materials with higher surface area, enlarged porous structure along with multi-phase coupling strategies enhance the charge transfer kinetics on the electrode surface and reduces the electrocatalytic activation energy barriers [17]. Developing a heterostructured electrocatalysts is a vital strategy in providing favorable active sites at closer proximities for catalytic activity enhancement [18]. Due to the fermi level equilibrium at the interface of two dissimilar metal, the charge depletion region is extended, which enhances charge transfer, inducing the synergistic effects within the matrix [19,20].

The abundant supply of Nickel (Ni) and its chemical stability, unique electronic structure, and enhanced synergistic interaction when coupling with other metals (like Ir, and Ru) makes it a promising candidate for heterostructure engineering of electrocatalysts [21]. The partially filled 3d orbital of Ni (II) ions were further split into two sub levels because of the crystal field effect of oxygen (O) ions around them. The upper 3d sublevel, which is partially filled, forms strong covalent bonds with neighboring O atoms, leading to the formation of improved characteristic oxidation states for electrocatalytic reactions [22]. This unique electronic structure of NiO plays a crucial role in its catalytic activity, making it a promising candidate for various electrochemical reactions. Also, the coupling of the double phase (Ni, Ir) and uniform atomic scale dispersion of metal atoms in a highly porous foam-like structure allows more favorable adsorption sites, leading to lower overpotentials with higher stability towards the half-cell reactions [17]. Even though iridium oxide proved to be an appropriate candidate for OER, the scarcity of Ir requires its optimized usage without compromising catalytic activity. Wang et al. showed that the development of single atom catalysts cannot provide overall catalytic efficiency due to single atom segregation and weak metal interaction. Still, this requires high loadings of ~18 and 11% to achieve overpotentials of ~215 and 257 mV when reaching a current density of 10 mA cm^{-2} [23]. The electrical contact interface of two dissimilar metals results in charge transfer and extending the charge depletion region, which acts as the basis for the synergistic effects [19,20]. In here, the NiO and IrO$_2$ corresponds to the two dissimilar metals and thus the creation of heterojunctions provides significant advantage over their unitary counterparts. The NiO/IrO$_2$-NF electrocatalyst utilizes the combined advantage of NiO and IrO$_2$ active sites with modulated electronic structure at the interface and intermediate absorption energy thus promoting the spontaneous electron transport during the catalytic reactions [24]. Additionally, the inclusion of NiO into IrO$_2$ proved to be effective in the utilization of Ir and their corresponding intrinsic catalytic activity [25,26].

Based on the above context, we fabricated a NiO/IrO$_2$-NF as an efficient trifunctional electrocatalyst using a simple yet effective solvothermal and calcination approach. There are no previous investigations on porous heterostructured NiO/IrO$_2$-NF electrocatalyst towards HER, OER and ORR reactions. Notably, the NiO/IrO$_2$-NF electrocatalyst displays an excellent OER performance with a minimum overpotential of about 240 mV at a current density of 10 mA cm^{-2}, significantly outperforming the commercial IrO$_2$ (280 mV). Also, the NiO/IrO$_2$-NF displayed enhanced performance towards HER with an overpotential of 42 mV (at 10 mA cm^{-2}) and ORR with a half wave potential ($E_{1/2}$) of 0.80 V. Individual reaction mechanistic pathways were investigated using density functional theory (DFT) calculations. The adsorption energies, density of states (DOS) and Gibbs free energy changes of the electrocatalysts during HER, OER and ORR were calculated. Further, the lab scale NiO/IrO$_2$-NF || NiO/IrO$_2$-NF water splitting device only required a 1.51 V cell voltage to reach a current density of 10 mA cm^{-2} with prolonged stability of 600 h (96% potential retention), significantly outperforming the commercial Pt/C || IrO$_2$ device. Further, a liquid electrolyte-based zinc air battery was fabricated with NiO/IrO$_2$-NF catalysts as the air cathode. The device displays an open circuit

voltage (OCV) of 1.55 V and enhanced power density of 134.8 mW cm^{-2} with 100 h of prolonged durability, outperforming the Pt/C+IrO$_2$ based air cathode. This rational development of highly porous, foam-like structured catalyst with electronic structure regulation and double phase coupling strategy provided a promising electrocatalyst for sustainable energy production via water splitting and zinc-air batteries.

2. Experimental section

2.1. Synthesis of foam like heterostructured NiIrO$_x$ (NiO/IrO$_2$-NF) electrocatalyst

All the scientific grade chemicals and reagents were used directly without any further purification. Initially, 4 g of glucose and 1 g of urea was mixed in 10 mL of DI water and sonicated for 1 h to obtain a clear homogeneous solution. Then, 8 mg of IrCl$_3$•xH$_2$O and 22.8 mg of NiSO$_4$•6 H$_2$O was added and sonicated until it is completely dissolved. Finally, the clear solution was heated at 160°C for 6 h to obtain a highly porous foam like structure. The rigid porous structure was collected and grinded to obtain a fine powder. Finally, the collected sample was calcinated at 400°C for 8 h in air medium to obtain the foam like heterostructured NiIrO$_x$ (NiO/IrO$_2$-NF). Similarly, IrO$_2$ (S-IrO$_2$; S indicates synthesized nanofoam like IrO$_2$) and NiO nanofoam (S-NiO) was synthesized using the same synthetic procedure without the addition of respective precursors and were investigated for comparative studies along with commercial IrO$_2$ and Pt/C. Using similar synthetic route, electrocatalyst with different mole ratios are prepared to optimize the electrochemical performance. In brief, Ni$_{1.5}$O/Ir$_{0.5}$O$_2$, and Ni$_{0.5}$O/Ir$_{1.5}$O$_2$ is named as NiO/IrO$_2$-NF-1 and 2, respectively.

2.2. Materials and electrochemical studies

Detailed descriptions of electrode fabrication and performance of the trifunctional electrocatalyst towards OER, ORR, and HER, along with overall water splitting device and zinc air battery fabrication are given in the supplementary information.

3. Results and discussion

3.1. Morphological and structural investigations of NiO/IrO$_2$-NF electrocatalyst

The NiO/IrO$_2$-NF and S-IrO$_2$ electrocatalyst was synthesized using a facile solvothermal and calcination technique with a sacrificial template approach as shown in Fig. 1a. Water-soluble glucose was used as the sacrificial template. Dissolved glucose gradually turns into molten syrup when the temperature increases to 160°C, and it controls the uniform distribution of the metal particles (Ni, Ir). Also, gas released during the decomposition of urea creates a porous foam in a blowing effect. In the calcination step, the sacrificial template was removed at 400°C to form highly porous NiO/IrO$_2$-NF. Thus, this synthetic process ensures the efficient distribution of individual metal elements within the structure aiding in enhancing the number of catalytic active sites. X-ray diffraction (XRD) analysis was employed to investigate the crystalline nature of the prepared electrocatalysts as shown in Fig. 1b. As-prepared heterostructured NiO/IrO$_2$-NF displayed stronger diffraction peaks at 28.03°, 34.70°, 37.2°, 40.05°, 43.29°, and 54.09° corresponding to (110), (101), (101), (200), (012) and (211), respectively. The observed XRD spectra agree with the standard JCPDS cards (no. 01–088–0288 and 01–089–7390) corresponding to IrO$_2$ and NiO, respectively. From the XRD results and the Scherrer equation, the average particle size was ~6 nm (±1 nm), and these results agree with the HR-TEM particle size findings [27]. XRD measurements before calcination showed no metal peaks due to the highly porous foam-like structure shown in Figure S1a. Additionally, Figure S1b shows the XRD pattern of S-IrO$_2$ where the primary NiO peaks were not observed. Since the catalyst was made of
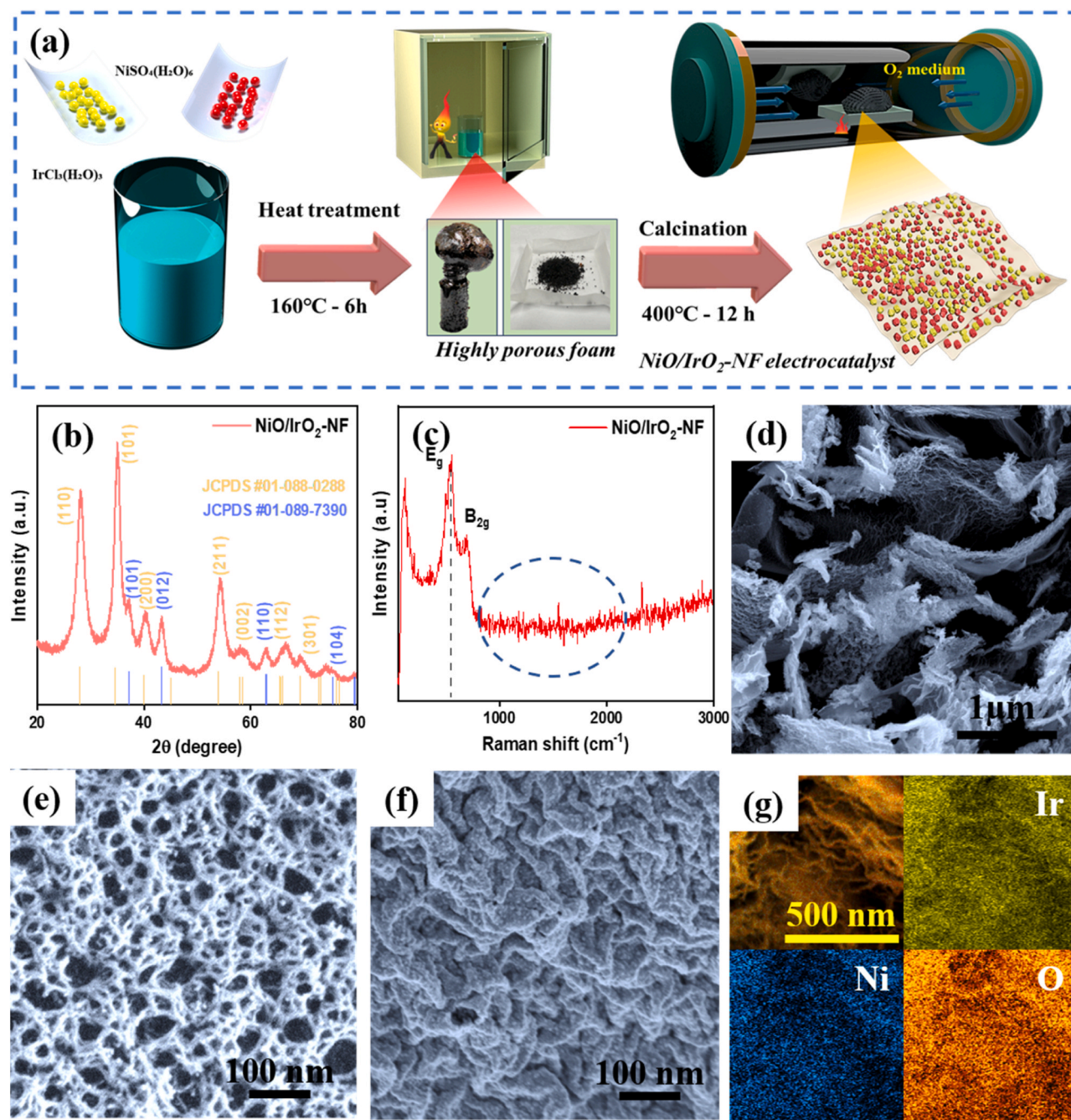
Fig. 1. (a) Schematic illustration of synthesis of NiO/IrO$_2$-NF and S-IrO$_2$ electrocatalysts, physio-chemical characterization: (b) XRD pattern with phase contribution of NiO/IrO$_2$-NF, (c) NiO/IrO$_2$-NF Raman spectra, (d-f) FE-SEM images of NiO/IrO$_2$-NF at different magnification, (g) particular area energy dispersive X-ray spectroscopy with individual element mapping of Ir, Ni, and O.

pure oxide, the carbon peak around 26° was absent, which is mainly attributed to the calcination of the porous foam at 400°C for 8 h. The absence of graphitic and defect peaks (D band/G band) in the Raman spectra further support this claim. The XRD characteristic peaks of NiO/IrO$_2$-NF show shift in their corresponding (200) and (110) peak position as compared to S-IrO$_2$, which indicates the change in lattice parameters of IrO$_2$ due to the inclusion of NiO [28,29].

Additionally, the Raman spectroscopy results in Fig. 1c confirmed the absence of D and G bands, corresponding to the defect and graphitic natures of the carbon in the electrocatalyst. Also, the dominant raman spectra at ~560 cm^{-1} (E$_g$) and 720 cm^{-1} (B$_{2g}$) well corresponds with the presence of IrO$_2$ in the S-IrO$_2$ electrocatalyst as shown in Figure S1c [30]. In NiO/IrO$_2$-NF, after the inclusion of NiO, the E$_g$ and B$_{2g}$ spectra

corresponds to IrO$_2$ shifts to lower frequency, as shown in Figure S1d, indicating the alteration in the local environment [31]. Fig. 1(d-g) shows the FE-SEM characterization of the prepared NiO/IrO$_2$-NF at different magnifications. Fig. 1d shows a uniform sheet-like structure was grown with the inclusion of Ni and Ir metal oxides. In higher magnification, Fig. 1(e-g) showed a sheet like structure with controlled pore size. Figure S2(a-d) displays additional FE-SEM images of NiO/Ir-O$_2$-NF electrocatalyst displaying uniform structural growth at higher magnifications. The presence of these surface area rich porous structures helped provide the active sites during the electrocatalytic reactions [32]. In addition, Fig. 1g shows the energy dispersive X-ray (EDAX) spectroscopy of NiO/IrO$_2$-NF electrocatalyst in a selected area, where the dual metal oxide particles were uniformly distributed within the

foam-like structure. EDS spectra revealed the composition of Ni, Ir, O in the particular area as shown in Figure S2e. Here, the individual sheets are formed by the accumulation and distribution of small particles, which is evident from the further higher magnification investigative results. Apart from a particular area mapping, line mapping investigations of S-IrO$_2$ and NiO/IrO$_2$-NF in Figure S3(a-b) show the controlled distribution of metal oxides and their corresponding intensity and elemental compositions.

Further intrinsic morphological characterization was carried out using TEM, HR-TEM and HAADF-STEM. Fig. 2(a-b) shows the morphologies of S-IrO$_2$, which show similar structural features to those of NiO/IrO$_2$-NF. After the inclusion of Ni, Fig. 2c shows the foam structure comprised of closely packed small crystals (Ir, Ni). The uniform foam structure is clearly observed as in FE-SEM results along with different

magnifications of TEM as shown in Figure S4(a-d). The particle size was calculated using ImageJ software, and the histogram in the inset Fig. 2c revealed the average crystal size was about 3–5 nm. Fig. 2(d-e) shows two different phases in the adjacent crystal units due to the formation of heterostructured nature, where the inset in Figure S4d displays the crystalline FFT (Fast Fourier Transform) pattern of NiO/IrO$_2$-NF. The inset in Fig. 2d shows the presence of multi-phase components with lattice distortions in the formed crystal units. Additionally, Figure S5(a-f) provides HR-TEM images of NiO/IrO$_2$-NF electrocatalyst confirming the presence of NiO and IrO$_2$ heterojunctions at different parts of the catalyst structure along with their corresponding d-spacing measurements. The obtained heterostructured phase formation of NiO/IrO$_2$-NF potentially reduced the charge transfer resistance in the electrical metal interface by providing a greater number of favorable adsorption sites
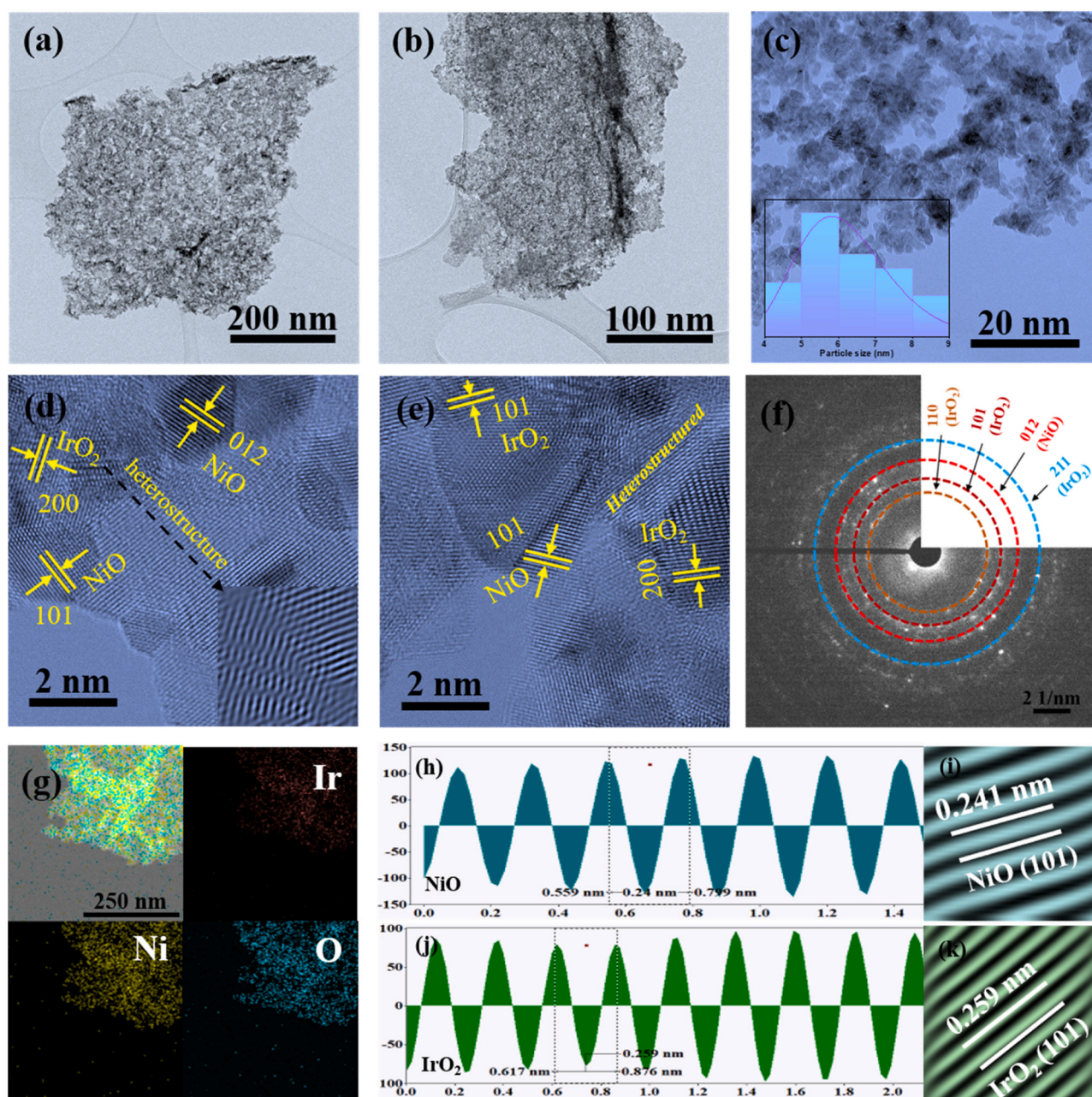

Fig. 2. Physiochemical characterization: TEM images of (a, b) S-IrO$_2$, (c) NiO/IrO$_2$-NF (inset shows the average crystal size histogram), (d, e) HR-TEM images of NiO/IrO$_2$-NF at different positions with dual phases (inset shows the enlarged heterostructured nature), (f) corresponding SAED pattern with respective crystal planes, (g) energy dispersive X-ray spectroscopy mapping of NiO/IrO$_2$-NF with individual elemental mapping, (h-k) lattice spacing with corresponding individual crystal planes.

[33]. It also aids in controlling the band structure and limits the intermediate activation barriers during catalytic reactions [20,34]. The polycrystalline nature of the NiO/IrO_2-NF is indicated by the bright crystalline rings (Fig. 2f) with d-spacing values corresponding to NiO_2 and IrO_2 phases of NiO/IrO_2-NF. Additionally, the HAADF-STEM elemental mapping in a selected area displayed a lower concentration of iridium atoms uniformly distributed throughout the structural lattice as shown in Fig. 2g along with the individual metal mapping to confirm the presence of metals throughout the sheet like structure. Also, the EDS spectrum shown in Figure S4e displays the distribution of Ir and Ni in the selected sectional area. Further, the HR-TEM image in Fig. 2(h-k) depicts lattice spacings and d-spacing values of 0.241 nm and 0.259 nm, respectively for the (101) planes of the NiO/IrO_2 heterostructured phase. Further, the lattice springe profile at two different places (Fig. 2(i and k)) shows the almost even spacing throughout the scan and their corresponding inverse FFT pattern profiles.

BET (Brunauer-Emmett-Teller) surface area was measured using N_2 adsorption isotherms to evaluate the porous nature of S-IrO_2 and NiO/IrO_2-NF electrocatalysts. The adsorption-desorption of NiO/IrO_2-NF porous nanoarchitectures at a relative pressure (P/P_0) with a hysteresis loop from 0.2 to 1.0 as shown in Figure S6(a-b). The investigative results revealed that the optimized NiO/IrO_2-NF displayed a significantly larger surface area of 58.71 m^2 g^{-1} as compared to S-IrO_2 (30.87 m^2 g^{-1}). It shows the inclusion of dual metal results in the creation of defects and the formation of a porous nature with larger surface area as shown in Figure S6b. Further, the pore size distribution in the prepared electrocatalysts was evaluated using the Barrett-Joyner-Halenda model. The NiO/IrO_2-NF had a mesoporous morphology as shown in inset Figure S6 (a-b), with a pore size distribution of around 30 nm, while the S-IrO_2 displays higher pore size (>50 nm). This heterostructured, mesoporous NiO/IrO_2-NF with a larger specific surface area and improved pore size provided enhanced reaction kinetics and catalytic active sites favoring the OER, HER, and ORR reactions [35].

The prepared electrocatalysts were examined using XPS (X-ray photoelectron spectroscopy) analysis to determine the chemical states and binding energies, and the results are shown in Fig. 3(a-e). The compared XPS survey spectrum in Figure S7a shows the presence of Ni 2p peaks after the inclusion of Ni, along with Ir 4 f, and O 1 s of NiO/IrO_2-NF electrocatalyst. The Ir 4 f spectra of S-IrO_2 was deconvoluted into two major peaks at 61.68 and 64.78 eV corresponding to $4f_{7/2}$ and
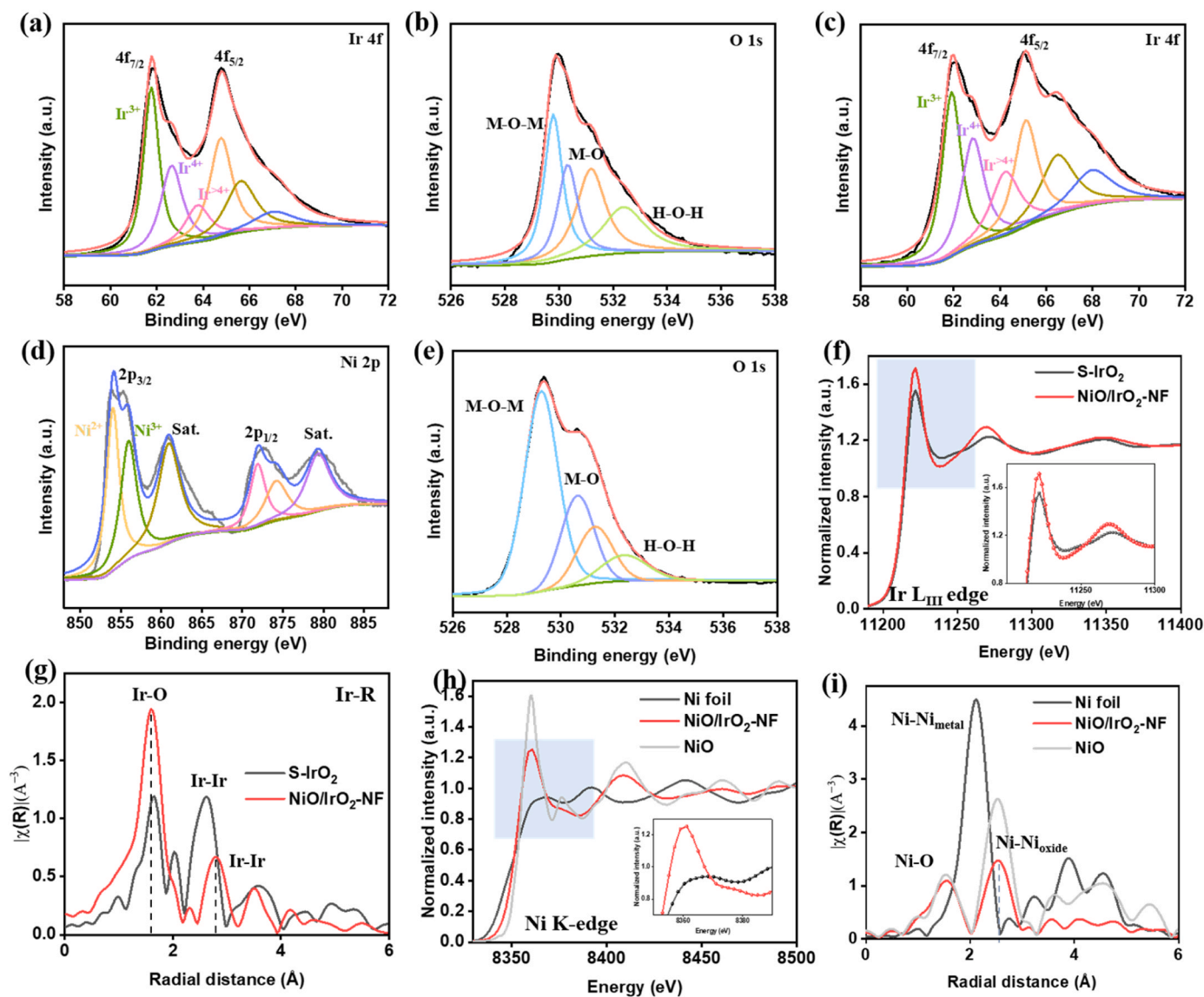

Fig. 3. XPS and XAS characterizations of S-IrO_2 and NiO/IrO_2-NF: (a) curve resolved XPS spectra of Ir 4 f, (b) O 1 s for S-IrO_2, (c) Ir 4 f, (d) Ni 2p, (e) O 1 s spectra of NiO/IrO_2-NF, (f) Ir L_{III}-edge XANES spectra of S-IrO_2 and NiO/IrO_2-NF, (g) Fourier-transformed EXAFS spectra at the corresponding Ir L-edge, (h) Ni K-edge based XANES spectra of Ni foil, NiO and NiO/IrO_2-NF, (i) corresponding FT-EXAFS spectra in R-space.

$4f_{5/2}$, respectively. The $4f_{7/2}$ peak of S-IrO$_2$ was further deconvoluted into three peaks at 61.58, 62.18, and 63.08 eV corresponding to Ir^{3+}, Ir^{4+}, and Ir$^{>4+}$, respectively. These indicate the presence of IrO$_2$ nanoparticles with higher oxidation states as shown in Fig. 3a. The O 1 s spectra of S-IrO$_2$ in Fig. 3b shows the metal oxide (M-O) peak at 529.8 eV and surface oxidative oxygen peak appearing at 530.38 eV [36]. Fig. 3c shows the high resolution Ir 4 f spectra of NiO/IrO$_2$-NF, where the binding energies of NiO/IrO$_2$-NF display a positive of about 0.35 eV (compared Ir 4 f spectra is shown in Figure S7c). This increase in binding energy along with increase in proportion of Ir^{4+} is mainly corresponds to the electron transfer and possible Ir-O bond formation at the heterointerface [37]. Along with the binding energy shift, the intensity of the Ir$^{>4+}$ spectra increased, indicating the change in oxidation states after the inclusion of Ni. The change in the oxidation state would decrease the Ir-O bond length, which provides enhanced OER activity due to the disruption of the IrO$_6$ octahedron [38,39]. Fig. 3d displays the deconvoluted high resolution spectra of Ni 2p with major peaks at 854.08 and 872.08 eV, which were further deconvoluted to a Ni^{2+} peak at 853.98 eV and a Ni^{3+} peak at 856.08 eV [40]. The peaks appearing at 860.98 and 879.48 eV appear to be satellite peaks (Sat.) [41]. Fig. 3e shows the deconvoluted O 1 s spectra of NiO/IrO$_2$-NF with a shift in binding energy, where the intensity of peak at 529.28 eV increased with respect to the increase in metal oxide interaction after the addition of Ni. Also, the increase in intensity of surface adsorbed oxygen provided electrochemical active sites and enhanced the surface activity during the catalytic reaction [42,43]. This confirmed the inclusion of the Ni into the host matrix along with higher metal-oxide interactions. The change in oxidation potential, metal oxide and metal-metal synergistic interaction can help improve the catalytic activity of the NiO/IrO$_2$-NF electrocatalyst [44].

To obtain better insight, S-IrO$_2$ and NiO/IrO$_2$-NF electrocatalysts were investigated using X-ray absorption spectroscopy (XAS) to understand their electronic configurations and elemental coordination. The L$_{III}$ edge, which is sensitive to the oxidation state changes in Ir, depicts the electron transition from filled 2p to unfilled 5d orbitals [45]. Fig. 3f shows the X-ray absorption near edge structure (XANES) spectra of S-IrO$_2$ and NiO/IrO$_2$-NF (Ir L$_{III}$ edge), revealing the slight edge energy shift (S-IrO$_2$ - 11215.78 to NiO/IrO$_2$-NF - 11216.74 eV). This indicates a decrease in average oxidation potential and presence of higher oxidation states in NiO/IrO$_2$-NF [46]. Also, the peak position of the white line stays in the same position indicating the presence of Ir^{4+} oxidation state in NiO/IrO$_2$-NF [47]. Further the extended X-ray adsorption fine structure (EXAFS) measurements, which show the interactions of X-rays with core level binding energy of atoms, provide more insight into the local coordination environment of the electrocatalysts and are shown in Fig. 3g. The compared FT-EXAFS spectra in Fig. 3g shows the surrounding oxygen atoms at ~1.55 A° (Ir-O) and the neighboring Ir atoms at ~2.5 A° (Ir-Ir), where its intensity decreases with the addition of new metal (Ni) into the S-IrO$_2$ matrix. The observable backscattering contributions around 2.5 A° corresponds to the metal like Ir-Ir interactions and around 3.3 A° indicates the oxidic Ir-Ir contributions [48,49]. Also, the smaller bond length of Ir-O in NiO/IrO$_2$-NF suggests the formation of higher redox states of iridium (Ir$^{>4+}$) [50]. Fig. 3h shows the Ni K-edge spectra with a pre-edge position at 8347 eV and main adsorption edge position at 8361 eV. The pre-edge energy shift indicates the presence of higher oxidation states, which is in agreement with the Ni 2p XPS results. The presence of multiple oxidation states affects the density of states (DOS) of the d orbital, which is proportional to the white line intensity. Also, the increase in white line intensity indicates a lower electron density and higher Ni oxidation states due to the increased number of unoccupied d orbitals. The Ni EXAFS fit in Fig. 3i shows the metallic Ni-Ni scattering in the range of 2.1 A° with a short bond distance corresponding to the Ni foil, tends to be increased in oxides due to the localization of electrons on oxygen atom with the addition of a coordinative shell (Ni-O). The Ni-O is shifted to a larger radius which in turn confirmed the presence of higher oxidation states in nickel atom.

[51] The Ni K-edge EXAFS fit in Figure S8a shows good agreement with the standard NiO fit with the existence of two distinct shell relative structurally to the radial function. The EXAFS fitting parameters and coordination numbers are represented in Table S1. For NiO/IrO$_2$-NF, the initial shoulder peaks in the first oxygen shell indicates the Ni-O coordination and the coordination shell around 2.5 A° corresponds towards the closest Ni-Ni distance between the two octahedral sites [52]. Similar to this, the K-edge (K$_3$ weighting) oscillation spectra in Figure S8(a-b) show better signal to noise ratios for the Ni and Ir of NiO/IrO$_2$-NF. The XAS results confirmed the formation NiO/IrO$_2$-NF with Ir-Ni interactions and the availability of rich oxidation states in Ni$^{>3+}$ and Ir$^{>4+}$ with lower electron density, which may lead to favorable redox reactions with enhanced electrocatalytic activity [53].

3.2. Electrochemical investigation of NiO/IrO$_2$-NF towards HER, OER and ORR

Evaluation of OER half-cell performance is crucial to understanding the performance of NiO/IrO$_2$-NF electrocatalysts towards water splitting and zinc-air batteries. All the electrochemical measurements were conducted using 1.0 M KOH electrolyte. To compare the obtained results, commercial IrO$_2$ electrocatalysts were also examined using similar fabrication methods with carbon paper. The recorded LSV curves were measured at a scan rate of 1 mV s^{-1} and were iR corrected using the standard equation. Since improper wetting causes fluctuations in catalytic performance, the catalyst coated carbon paper was immersed in the electrolyte solution for 30 mins to ensure complete wetting. Prior to experimental evaluation, the hydrophilic nature of the prepared electrocatalysts on the carbon paper was investigated using contact angle measurements shown in Figure S9(a-d). The results imply that the NiO/IrO$_2$-NF exhibits a lower contact angle of 37°, indicating the significant hydrophilic nature in contrast to other catalysts, which facilitates the electron/ion movement. The LSV curves in Fig. 4a show that the optimal NiO/IrO$_2$-NF catalyst displays a smaller overpotential of about 240/330 mV at a current density of 10/100 mA cm^{-2} as compared to S-NiO (390/650 mV), S-IrO$_2$ (298/540 mV), IrO$_2$ (263/400 mV) and most of the recently reported electrocatalyst (Table S2). For optimization, electrocatalysts with different mole ratio are investigated under similar conditions and the results shows NiO/IrO$_2$-NF-1 and NiO/IrO$_2$-NF-2 displays an overpotential of 280 mV, and 244 mV as shown in Figure S10a. Tafel slope was evaluated from a plot of log (j) vs. overpotential (η) from the obtained LSV curves, and the results are shown in Fig. 4b. The results reveals that the optimal NiO/IrO$_2$-NF shows a smaller Tafel value of 64 mV dec^{-1} in comparison to S-NiO (91 mV), S-IrO$_2$ (74 mV dec^{-1}) and commercial IrO$_2$ (71 mV dec^{-1}). Similarly, Figure S10b shows that the NiO/IrO$_2$-NF-1 and NiO/IrO$_2$-NF-2 displaying a Tafel values of 64 mV dec^{-1}, 76 mV dec^{-1} and 65.2 mV dec^{-1}, respectively. Additionally, all the electrocatalysts were investigated in 0.1 M KOH medium to understand the bifunctional property towards the zinc-air battery. LSV curves in Figure S11a showed that the NiO/IrO$_2$-NF displayed a lower overpotential of 272 mV to reach the current density of 10 mA cm^{-2}, outperforming the S-IrO$_2$ (335 mV) and commercial IrO$_2$ (297 mV). Also, the NiO/IrO$_2$-NF displayed faster reaction kinetics with lower Tafel slope value of (61 mV dec^{-1}) than S-IrO$_2$ (75 mV dec^{-1}) and IrO$_2$ (68 mV dec^{-1}) as in Figure S11c. The heterojunctions of NiO and IrO$_2$ provided faster electron transport at their interfaces resulting in improved reaction kinetics and lower Tafel values of NiO/IrO$_2$-NF [54]. The excellent OER activity with favorable reaction kinetics is mainly attributed to the double phase synergistic interactions and the porous foam nature that provides enhanced active sites for *OH adsorption, which reduce the OER activation energy barrier [55]. This larger number of active sites helps the catalyst to obtain larger current density with minimum overpotential.

The ion transport and conductivity of the prepared electrocatalyst were evaluated using the electrochemical impedance spectra (EIS) as shown in Figure S12(a-d). The optimal NiO/IrO$_2$-NF nanofoam has a
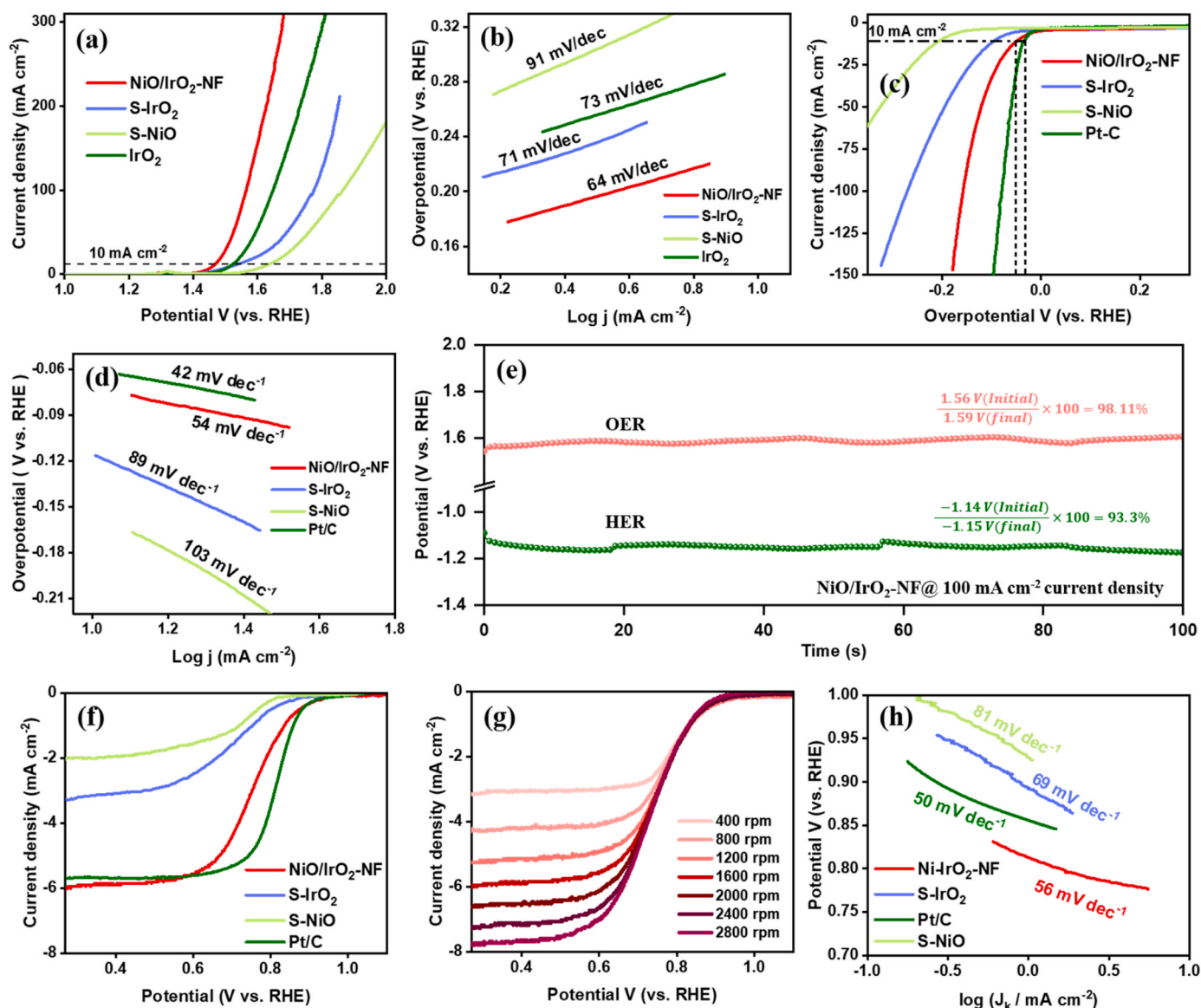
Fig. 4. Electrochemical half-cell investigations (a) OER LSV curves for NiO/IrO$_2$-NF, S-IrO$_2$, S-NiO and IrO$_2$, (b) corresponding OER Tafel values, (c) HER polarization curves for NiO/IrO$_2$-NF, S-IrO$_2$, S-NiO and Pt-C, (d) HER Tafel values, (e) chronopotentiometric curves of NiO/IrO$_2$-NF towards HER and OER for 100 h at a current density of 100 mA cm^{-2}, (f) compared ORR LSV curves at a scan rate of 10 mV s^{-1}, (g) LSV curves of NiO/IrO$_2$-NF catalyst at a different rotational speeds of 400–2800 rpm, (h) corresponding Tafel values.
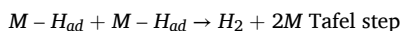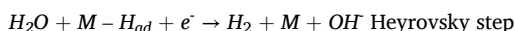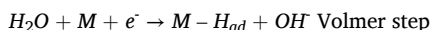
smaller R$_{ct}$ value of 2.1 Ω as compared to S-NiO (6.3 Ω), S-IrO$_2$ (4.2 Ω) and commercial IrO$_2$ (2.9 Ω). Similar charge transfer resistance characteristics are displayed in the 0.1 M KOH medium as shown in Figure S11d. Then, CVs with different scan rates were recorded in the non-faradaic region to evaluate the electrochemically active surface area (ECSA) as shown in Figure S13(a-d). The results show that the C$_{dl}$ values of NiO/IrO$_2$-NF, S-NiO, S-IrO$_2$ and IrO$_2$ were about 18.7 mF cm^{-2}, 11.7 mF cm^{-2}, 14.9 mF cm^{-2} and 14.2 mF cm^{-2}, respectively. Based on these C$_{dl}$ values, the ECSA of the NiO/IrO$_2$-NF was found to be 467.5 cm^2, which is higher than the S-NiO (292.5 cm^2) S-IrO$_2$ (372 cm^2) and commercial IrO$_2$ (355 cm^2) as shown in Figure S13i. Higher electrochemical active sites in the NiO/IrO$_2$-NF were mainly due to its intriguing heterostructured, mesoporous, and defect-rich nature. To better understand the intrinsic activity the measured LSV curves are normalized with the corresponding ECSA values as shown in Figure S13j. Additionally, the LSV curves are normalized with noble metal loading to illustrate the utilization of noble metal in the electrocatalysts (Figure S13k). Additionally, the turnover frequency (TOF), a

critical electrochemical efficiency marker, was evaluated using the standard equations at an overpotential of 420 mV, as shown in the supporting information. Also, the individual metal composition, to calculate TOF, was evaluated using ICP-OES (Inductive coupled plasma optical emission spectroscopy) and the metal percentage is shown in Figure S14. The optimized NiO/IrO$_2$-NF electrocatalyst exhibited a significantly higher TOF value of 0.0414 s^{-1} as compared to the S-IrO$_2$ (0.02711 s^{-1}). These results indicate that the optimal NiO/IrO$_2$-NF electrocatalyst provides favorable thermodynamics and faster reaction kinetics towards OER activity.

Apart from outstanding OER activity, the integrity and robustness of the optimal NiO/IrO$_2$-NF electrocatalyst was investigated using log-term durability, cyclic stability, and multi-step chronopotentiometry analysis in a 1.0 M KOH medium. Fig. 4e shows the prolonged durability of NiO/IrO$_2$-NF with minimal change in voltage fluctuations for 100 h at a constant current density of 100 mA cm^{-2}. Similarly, the durability of NiO/IrO$_2$-NF-1,2 is shown in Figure S10c. Post durability LSV curves in Figure S15a showed a minimal change of ~8 mV (around 5% loss) after

the 100 h stability test. Further, the NiO/IrO$_2$-NF was subjected to 1000 CV cycles at a scan rate of 100 mA s^{-1} as shown in Figure S15b and Figure S15c show the recorded multi-step potentiometry with current densities varied randomly from 10 to 160 mA cm^{-2}. Even after applying high current densities at different intervals to simulate an input fluctuation with harsh working conditions, the NiO/IrO$_2$-NF retains its initial activity after 10 h without any significant loss.

In addition to excellent OER activity, the optimized NiO/IrO$_2$-NF was investigated for HER in a cathodic half-cell reaction in overall water splitting. Like the OER, all the measurements were investigated in 1.0 M KOH electrolyte at a scan rate of 1 mVs^{-1}. The LSV curves of prepared electrocatalysts are compared in Fig. 4c. The results revealed that the optimal NiO/IrO$_2$-NF displays a smaller overpotential of 42 mV as compared to S-IrO$_2$ (90 mV) and (20% Pt) Pt/C (36 mV). Also, the NiO/IrO$_2$-NF-1 and NiO/IrO$_2$-NF-2 electrocatalyst displays an overpotential of 74 mV and 53 mV, respectively as shown in Figure S16a. The Tafel values from the recorded LSV curves were calculated and are shown in Fig. 4d. As shown, the optimal NiO/IrO$_2$-NF displays a smaller Tafel value of 54 mV dec^{-1} than the S-IrO$_2$ (84 mV dec^{-1}), which is comparable to the benchmark Pt/C (42 mV dec^{-1}) and recently reported HER electrocatalysts shown in Table S3. Figure S16b shows the Tafel slope values of NiO/IrO$_2$-NF-2/3 electrocatalysts as 71/61 mV dec^{-1}. Here, the HER might take place via two possible reaction pathways:

$$H_2O + M + e^- \rightarrow M - H_{ad} + OH^- \text{ Volmer step}$$

$$H_2O + M - H_{ad} + e^- \rightarrow H_2 + M + OH^- \text{ Heyrovsky step}$$

$$M - H_{ad} + M - H_{ad} \rightarrow H_2 + 2M \text{ Tafel step}$$

Initial hydrogen adsorption (Volmer step) is required in both reaction pathways. Further, the evolution of hydrogen can occur via the Heyrovsky step or the Tafel step. The evaluated Tafel values showed that the optimal NiO/IrO$_2$-NF governs the Volmer-Heyrovsky reaction pathway. Additionally, the EIS results in Figure S10(d-f) show that the optimal NiO/IrO$_2$-NF displays a lower Rct value of 2.9 Ω as compared to S-NiO (5.9 Ω), S-IrO$_2$ (4.2 Ω) nanofoam and Pt/C (3.3 Ω). The smaller Tafel and Rct values showed the enhanced reaction kinetics and faster electron transport properties with favorable reaction thermodynamics of optimal NiO/IrO$_2$-NF towards HER. Non-faradaic region CV measurements were recorded and evaluated, as shown in Figure S17(a-d). The resulting linear relationship for different scan rates shows that NiO/IrO$_2$-NF exhibits a C$_{dl}$ value of 30.2 mF cm^{-2}, outperforming the commercial Pt/C (27.15 mF cm^{-2}), S-IrO$_2$ (13.6 mF cm^{-2}) and S-NiO (10.3 mF cm^{-2}). From this, the ECSA values were calculated and found to be 755, 678.8, 340 cm^{-2} and 257.5 mF cm^{-2} for NiO/IrO$_2$-NF, Pt/C, S-IrO$_2$ and S-NiO, respectively a shown in Figure S17i. Further, the measured LSV curves are normalized with the corresponding HER ECSA values as shown in Figure S17j. Also, the LSV curves are normalized with noble metal loading to illustrate the utilization of noble metal in the electrocatalysts (Figure S17k). Similar to OER, NiO/IrO$_2$-NF outperformed the commercial electrocatalysts due to its intriguing properties. Subsequently, TOF values of all the prepared electrocatalysts were calculated to evaluate the active sites and their electron transport kinetics during HER. The optimal NiO/IrO$_2$-NF showed a higher TOF value (0.0327 s^{-1}) than S-IrO$_2$ (0.0276 s^{-1}) at an overpotential of 290 mV. Apart from intrinsic activity, the durability and stability of the optimal NiO/IrO$_2$-NF was evaluated using chronopotentiometry measurements in 1.0 M KOH medium. Fig. 4e shows the long-term durability curves of NiO/IrO$_2$-NF for around 100 h with insignificant fluctuations at a constant current density of 100 mA cm^{-2}. Likewise, the durability of NiO/IrO$_2$-NF-1,2 is shown in Figure S16c. Post durability LSV measurements in Figure S18a showed minimal loss of ~6 mV (10%), demonstrating the robustness and structural integrity of the optimal catalyst. Further, the cyclic stability with 1000 cycles at a constant scan rate of 100 mV s^{-1} was measured, and the results display minimal loss as shown in Figure S18b. Additionally, the multi-step chronopotentiometry was performed with

current densities 10–100 mA cm^{-2}. The results in Figure S18c show the retention of initial activity even after being subjected to high current density. The results show the enhanced catalytic activity of optimal NiO/IrO$_2$-NF electrocatalyst towards the HER in an alkaline medium.

Motivated by the excellent OER and HER results, the NiO/IrO$_2$-NF was investigated for its ORR performance in N$_2$ and O$_2$ saturated 0.1 M KOH electrolyte. To compare the activity, commercial state of the art Pt/C (20% Pt) was coated on a rotating disk electrode (RDE) with similar catalyst loading. Figure S19a shows the ORR cyclic voltammetry curves of NiO/IrO$_2$-NF in N$_2$ and O$_2$ medium, where no reduction peak was observed in the N$_2$ saturated electrolyte. The cathodic reduction peaks appeared when the electrolyte was saturated with O$_2$, indicating the ORR activity. A comparison of LSV curves in Fig. 4f show the NiO/IrO$_2$-NF exhibiting a half-wave potential of about 0.80 V (E$_{1/2}$=0.80 V), which is significantly higher than S-IrO$_2$ (E$_{1/2}$=0.70 V), S-NiO (E$_{1/2}$=0.68 V) and comparable to the commercial Pt/C (E$_{1/2}$=0.85 V) and recently reported ORR catalysts (Table S4). Figure S19b shows the LSV curves of NiO/IrO$_2$-NF-1,2 displaying half-wave potential of 0.75 V and 0.78 V, respectively. Further, Fig. 4g shows the LSV curve of NiO/IrO$_2$-NF in 0.1 M KOH (O$_2$ saturated) electrolyte with rotation speeds of 400–2800 rpm. All the recorded LSV curves (O$_2$ saturated) were corrected using the response measured from the N$_2$ saturated blank response. The LSV curves in Fig. 4g show an increase in diffusion limited current density proportional to the rotation speed (400–2800 rpm), indicating the enhanced mass transfer kinetics at higher rotation speeds [56,57]. Also, the dual metal active sites with enriched surfaces provided a greater number of favorable adsorption sites in closer proximities without the aggregation on the active sites, which increased the ORR activity of the NiO/IrO$_2$-NF electrocatalyst. The Tafel slope is an intrinsic activity marker for the evaluation of reaction pathway and kinetics of the electrochemical reaction, and it is shown in Fig. 4h and Figure S19c. NiO/IrO$_2$-NF demonstrated a lower Tafel value of 60 mV dec^{-1}, which is comparable to the commercial Pt/C electrocatalyst (57 mV dec^{-1}). This result supports the enhanced ORR catalytic activity of the optimal NiO/IrO$_2$-NF alongside other half cell reactions. Here, the nanofoam structure with larger surface area provides more active sites, reducing the activation energy barrier for ORR along with efficient electron transport kinetics [58]. The number of electrons transferred during the reaction was measured using a K-L (Koutecky-Levich) plot, which acts as the indicator for the ORR reaction mechanism. Figure S19d shows the evaluated K-L plot for NiO/IrO$_2$-NF in the potential range of 0.4–0.7 V to measure the transferred electrons, which also show the linear proportionality of current density towards the RDE rotational speeds [59]. These results show an electron transfer number of 3.9 (n), indicating first order kinetic behavior. This also confirmed that the conversion of O$_2$ to H$_2$O during the ORR was by the 4 electron (4e$^-$) transfer ORR pathway. Finally, the durability of the catalyst was evaluated using chronopotentiometry measurements at a constant potential of ~0.67 V as shown in Figure S19e. The retention efficiency of NiO/IrO$_2$-NF was more than 80% after a 25 h durability test, demonstrating the structural integrity of the optimal electrocatalyst. Finally, the bifunctional behavior of the NiO/IrO$_2$-NF towards OER/ORR was evaluated using the E value (ΔE=E$_{j=10(OER)}$-E$_{1/2(ORR)}$), which was around ~0.68 V. The evaluated potential window (E=0.68 V) is inversely proportional to the efficiency of the electrocatalysts. This becomes evident that the optimal NiO/IrO$_2$-NF shows exceptional catalytic activity and stability towards ORR. From the half-cell investigations it becomes clear that the synergistic interaction between NiO and IrO$_2$ in the heterostructures provides a strategical advantage for the NiO/IrO$_2$ NF electrocatalyst as compared to their respective unitary components i. e., S-IrO$_2$ and S-NiO.

3.3. Density function theory (DFT) calculations

The tetragonal unit cell of IrO$_2$ (JCPDS #01–088–0288) in the space group P42/mnm was optimized in the Brillouin zone sampling of 7×7x7,

Monkhorst-Pack K-Points with lattice constants a = b = 4.4983 Å, c = 3.1547Å, and angles α = β = γ = 9$\overset{\circ}{0}$. Then, we constructed an IrO$_2$ (110) model and applied a vacuum depth of 15Å in the z-direction. Similarly, the rhombohedral unit cell of NiO (JCPDS #01–089–7390) in the space group R-3 m was optimized in the Brillouin zone sampling of 7x7x7 Monkhorst-Pack K-Points with lattice constants a = b = 2.9549 Å, c = 7.2266 Å, and angles α = β = 9$\overset{\circ}{0}$, γ = 12$\overset{\circ}{0}$. Then, we constructed NiO (012) slab and applied a vacuum depth of 15Å in the z-direction. The NiO/IrO$_2$-NF heterostructure was constructed from IrO$_2$ (110) and NiO (012) slabs. To find the most active regions, different surface sites were constructed in the NiO/IrO$_2$-NF electrocatalyst. The NiO/IrO$_2$-NF heterostructure was assembled based on experimental data. During structure optimization, the half layers of NiO, IrO$_2$ and NiO/IrO$_2$-NF were relaxed, and the remaining half layers were fixed, Figure S20 represents the optimized structures of NiO (012), IrO$_2$(110), and NiO/IrO$_2$-NF electrocatalyst. The calculated formation energy (E$_F$) values in Table S6 show that the formation energy of NiO/IrO$_2$-NF is more negative −5.477 eV as compared to NiO (-4.751 eV) and IrO$_2$ (-4.836 eV). This indicates that the NiO/IrO$_2$-NF structure is a more stable electrocatalyst.

The density of states (DOS) and Gibbs free energy change of hydrogen adsorption (ΔG$_{H*}$) are crucial for understanding the performance of an electrocatalyst. Catalysts with higher DOS values near the Fermi level are expected to exhibit greater conductivity [60]. The Gibbs free energy change of hydrogen adsorption on a good HER catalyst is close to zero (0 eV) [61]. Therefore, we calculated the DOS and Gibbs free energy changes (ΔG$_{H*}$) of the S-NiO, S-IrO$_2$ and NiO/IrO$_2$-NF electrocatalysts. Figure S21 shows that NiO/IrO$_2$-NF has a higher spin-polarized density of states around the Fermi level than S-NiO and S-IrO$_2$. This suggests that the electronic structure of NiO/IrO$_2$-NF has more electronic states near the Fermi energy level, resulting in significant improvement and numerous charge carriers. This higher mobility and conductivity within the transport system may contribute to the excellent catalytic activity of NiO/IrO$_2$-NF. To identify the main active sites of the catalyst, we examined H*-atoms adsorbed on the NiO/IrO$_2$-NF heterostructure at various positions as shown in Figure S22. The Gibbs energy changes at each site were 0.099 eV (Ir), 0.193 eV (Ni), and 0.618 eV (O), respectively. The Gibbs free energy (ΔG$_{H*}$) value of NiO/IrO$_2$–NF on the Ir-active site is 0.099 eV, closer to 0 eV compared to NiO and IrO$_2$ materials. This indicates that NiO/IrO$_2$-NF has outstanding performance for HER activity, as illustrated in Table S6 and Fig. 5a.

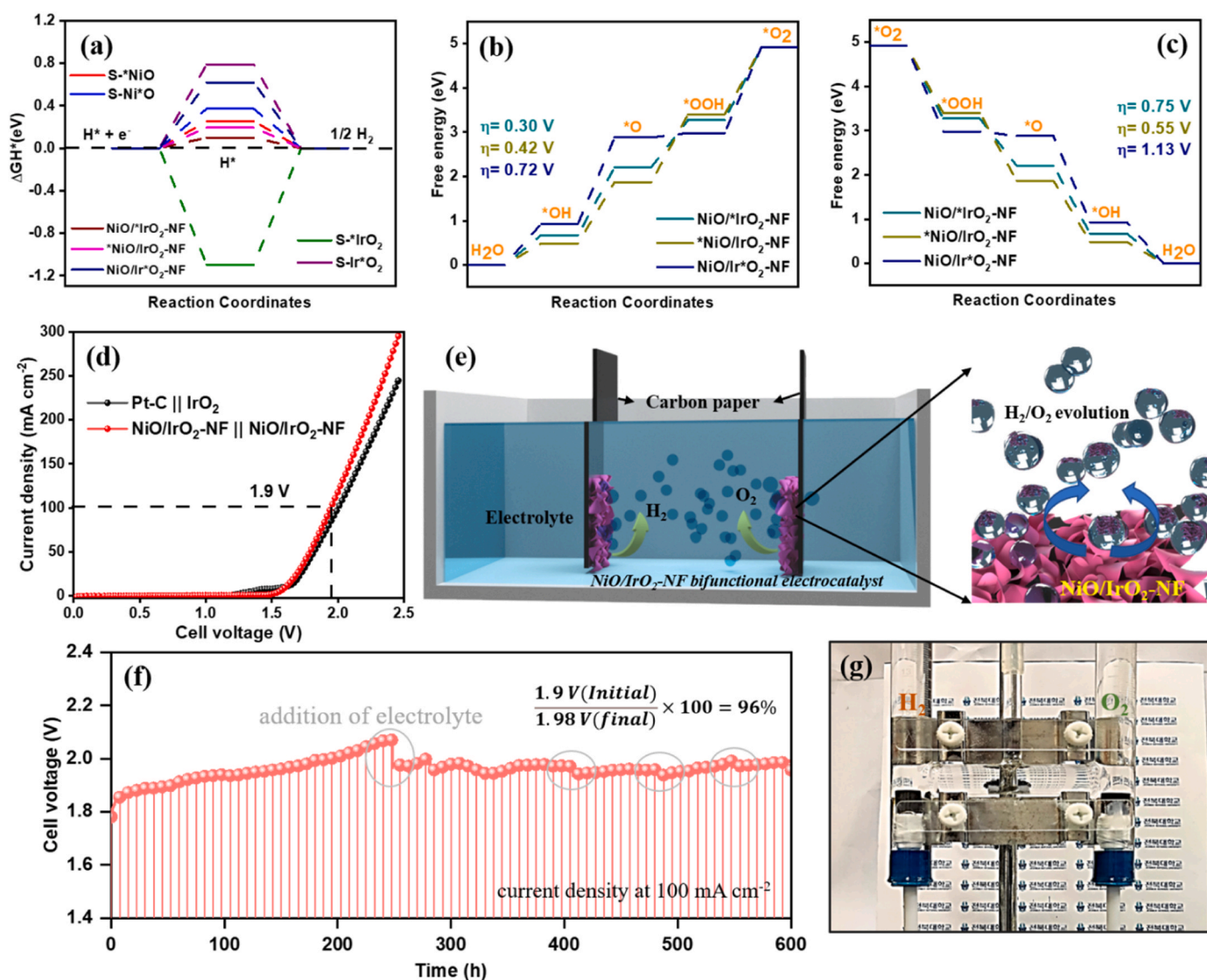To evaluate the theoretical overpotential (η) and the free energy

Fig. 5. Calculated free energy diagrams and reaction pathways for (a) HER, (b) OER, and (c) ORR for NiO/IrO$_2$-NF, S-IrO$_2$ and S-NiO electrocatalysts. Overall water splitting performance: (d) LSV curves of NiO/IrO$_2$-NF || NiO/IrO$_2$-NF and Pt/C || IrO$_2$, (e) schematic illustration of bifunctional water splitting device, (f) ultra-long durability results of NiO/IrO$_2$-NF || NiO/IrO$_2$-NF for 600 h at a constant current density of 100 mA cm^{-2}, (g) photographic display of faradaic measurement device.

changes (ΔG) in the oxygen evolution reaction (OER) and oxygen reduction reaction (ORR), the corresponding mechanistic pathways were calculated as shown in Table S7 and S8. In the OER, it is crucial to recognize the adsorption ability of the electrocatalyst. To calculate the theoretical overpotential, the Gibbs free energy changes (ΔG_T) in the reaction steps of the four-electron mechanism were calculated as shown in Fig. 5b, S23, S24, S25 (a, c) and Table S7. Among the various active sites, the Ir site is responsible for the superior OER performance in NiO/IrO$_2$-NF with the lowest overpotential (0.30 V). The formation of OOH* from O* is a rate-determining step in the OER process at the Ir active sites of NiO/IrO$_2$-NF, whereas the conversion of OOH* into O$_2$ and OH* into O* species has a maximum energy barrier at the other sites "Ni" and "O" of NiO/IrO$_2$-NF, respectively. The calculated overpotential (η_{OER}) of NiO/IrO$_2$-NF was 0.30 V, which is lower than S-NiO (0.95 V) and S-IrO$_2$ (0.42 V), which implies that OER occurs more easily at Ir active sites of NiO/IrO$_2$-NF. The oxygen reduction reaction (ORR) is a reversible process of OER. Reactions steps in ORR are all downhill of S-NiO, S-IrO$_2$, and NiO/IrO$_2$-NF, as shown in Fig. 5c, Figure S25 (b, d), and Table S8. The Ni-active site in NiO/IrO$_2$-NF demonstrates the best performance for ORR with the lowest overpotential (0.55 V) as compared to other active sites. The DFT results confirmed that the heterostructure NiO/IrO$_2$-NF exhibits outstanding performance as a trifunctional electro-catalytic in HER, OER, and ORR.

3.4. Overall water splitting

As the NiO/IrO$_2$-NF electrocatalyst displayed excellent OER and HER performances, a water electrolyzer was fabricated and evaluated in 1.0 M KOH electrolyte. To compare the performance, NiO/IrO$_2$-NF || NiO/IrO$_2$-NF and Pt/C || IrO$_2$-based water electrolyzer performances were measured and compared. The LSV curve of NiO/IrO$_2$-NF || NiO/IrO$_2$-NF based water electrolysis device achieved a cell voltage of 1.52 V at a current density of 10 mA cm^{-2} as shown in Fig. 5d, which is comparably higher than commercial Pt/C || IrO$_2$ (1.54 V at a current density of 10 mA cm^{-2}). Fig. 5e shows the schematic illustration of fabricated lab scale water electrolyzer using carbon paper as the working substrate along with the evolution of H$_2$/O$_2$ from the corresponding electrodes. The NiO/IrO$_2$-NF || NiO/IrO$_2$-NF water electrolyzer was also subjected to chronopotentiometry measurements at a constant current density of 100 mA cm^{-2} for 600 h. Surprisingly, Fig. 5f shows the stability curve with minimal fluctuations for 600 h (24 days), and the LSV curve measured after the stability test showed minimal change in overpotential ± 10 mV (~97% retention). As-prepared NiO/IrO$_2$-NF electrocatalyst stand out in providing a prolonged durability (600 h) as compared to many of the recently reported trifunctional electro-catalysts. Additionally, the evolution of H$_2$ and O$_2$ was measured using the water displacement method to evaluate the faradaic efficiency of NiO/IrO$_2$-NF as shown in Fig. 5g. The results in Figure S26(a-c) show a faradaic efficiency of 97 and 95% for H$_2$ and O$_2$, respectively. To examine the structural and chemical changes after 600 h durability tests, NiO/IrO$_2$-NF electrocatalyst was examined via TEM, HR-TEM, HAADF-STEM, and XPS analysis. Figure S27(a-b) shows the CS-TEM images, indicating the structural retention after prolonged durability tests of NiO/IrO$_2$-NF electrocatalyst on the anodic side, and the inset FFT pattern shows its crystalline nature. HR-TEM images show the presence of lattice spacings corresponding to the NiO and IrO$_2$ as shown in Figure S27(c-d). Further, the HAADF-STEM elemental mapping indicates the presence of Ir, Ni, and O uniformly distributed along with their elemental composition in that measured area (Figure S27(e-f)). The results indicate further oxidation of the NiO/IrO$_2$-NF electrocatalyst during the OER stability measurements. Similarly, Figure S28(a-b) shows the structural retention of cathodic NiO/IrO$_2$-NF electrocatalyst after 600 h durability measurement. HR-TEM images with corresponding lattice spacings of NiO and IrO$_2$ displays the presence of heterostructured nature in Figure S28(c-d). Further the elemental mapping shows the presence of individual elements with significantly lower

oxidation occurrence (Figure S28(f-g)). XPS survey spectrum in Figure S29a confirmed the presence of individual elements with slight changes in their intensity. High resolution spectra of Ir 4 f (Figure S29b) showed the change in intensity of Ir^{3+} with shift in binding energy, which is mainly due to its active involvement in the reaction. Similarly, Ni 2p high resolution spectra showed an insignificant change in intensity and binding energy of Ni^{3+} as shown in Figure S29c. During the reduction reaction, the metal-based catalyst does not undergo any significant phase transformation and thus the NiO/IrO$_2$-NF showed insignificant changes after stability measurements [62]. These post-morphological investigative results indicate the maximum retention of Ir and Ni active sites along with structural robustness of the NiO/IrO$_2$-NF electrocatalyst. This strategical synthesis of dual phase coupled NiO/IrO$_2$-NF resulted in a potential candidate for developing ultra-durable water electrolyzer devices in future energy storage and conversion systems.

3.5. Zinc-air battery performance

Inspired from the excellent OER and ORR half-cell reactions, a liquid electrolyte-based rechargeable zinc-air battery was fabricated using the NiO/IrO$_2$-NF electrocatalyst as the air cathode. In this, the carbon paper coated with NiO/IrO$_2$-NF electrocatalyst (~3 mg) was used as the air cathode along with commercial zinc foil as the anode and a liquid electrolyte of 0.2 M Zn (OAc)$_2$ + 6 M KOH. Fig. 6a shows the schematic illustration of the fabricated zinc-air battery assembly. The fabricated NiO/IrO$_2$-NF air cathode battery displays an open circuit voltage (OCV) of ~1.55 V for 8 h as shown in Figure S30a. For comparison, a commercial Pt/C+IrO$_2$ (1:1 ratio) air cathode was fabricated using a similar procedure, which and shows an OCV of ~1.43 V. The NiO/IrO$_2$-NF air cathode-based zinc-air battery displayed a power density of 134.8 mW cm^{-2}, which was significantly higher than the commercial state of the art Pt/C+IrO$_2$ (58 mW cm^{-2}) as shown in Fig. 6b and S30b. The specific capacity of the zinc-air battery was calculated from the zinc mass consumption at the anode as shown in Fig. 6c, and the results show NiO/IrO$_2$-NF displays a higher specific capacitance of 726 mAh g^{-1} than Pt/C+IrO$_2$ (584 mAh g^{-1}). Fig. 6d displays the dual functional efficiency indicator ($\Delta E = E_{j=10(OER)}$-$E_{1/2(ORR)}$), where a minimum energy difference of 0.70 V was observed. In a practical example, assembled zinc-air batteries were connected in series to power a red LED as shown in Fig. 6e. Galvanostatic charge-discharge curves with 5 mins charge and discharge cycle at a constant current density (2/5/10 mA cm^{-2}) were investigated to examine the zinc-air battery durability. The NiO/IrO$_2$-NF zinc-air battery shows an initial round trip overpotential of 0.75 V with an efficiency of 64%. After 100 h, the round trip overpotential increased to 0.78 V with 59.5% round trip efficiency, whereas the Pt/C+IrO$_2$ displays significantly lower durability as shown in Fig. 6f. Similarly, Figure S31(a-b) shows the NiO/IrO$_2$ air cathode-based zinc-air battery cycling stability at higher current densities of 5 and 10 mA cm^{-2} with 5 mins charge discharge cycles. A heterostructured surface with a higher surface area and synergistic interactions between metal oxides of NiO/IrO$_2$-NF provided faster charge transfer and reaction kinetics resulting in enhanced zinc-air battery performance. Further, Fig. 6g displays two NiO/IrO$_2$-NF based zinc-air batteries coupled with the NiO/IrO$_2$-NF-based water electrolyzer device as a prototype of a sustainable self-powered hydrogen production model. Fig. 6h shows the single NiO/IrO$_2$-NF-based rechargeable liquid zinc-air battery, which displays an OCV of 1.55 V. The performance and durability findings clearly depict the viability of using NiO/IrO$_2$-NF electrocatalysts as air cathodes for rechargeable zinc air battery applications.

Further, NiO/IrO$_2$-NF was investigated using FE-SEM, TEM, HR-TEM, and XPS to understand the structural and binding energy changes that occurred after the 100 h charge discharge test. Fig. 7(a-b) and S32(a-f) show the structural retention of the electrocatalysts after the constant charge discharge along with its crystalline nature. Interestingly, the heterostructured nature remains intact, indicating that no
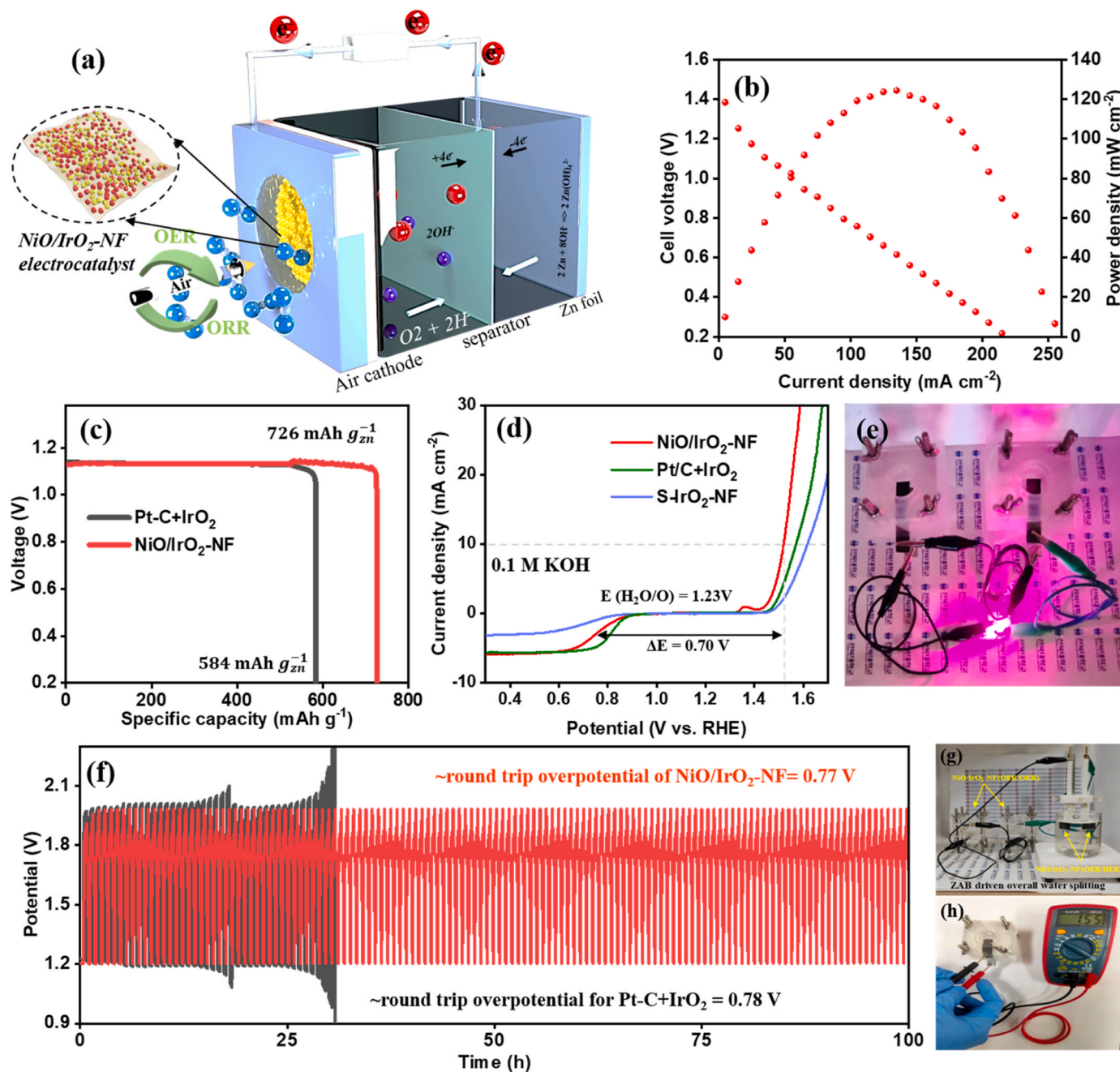
Fig. 6. Zinc-air battery performance. (a) Schematic illustration of zinc air battery using NiO/IrO$_2$-NF as the air cathode, (b) discharge polarization and corresponding power density curve of fabricated zin-air battery, (c) specific capacity of zinc–air batteries with NiO/IrO$_2$-NF and Pt/C+IrO$_2$ based air cathode at 10 mA cm^{-2}, (d) bifunctional (OER/ORR) performance of NiO/IrO$_2$-NF in 0.1 M KOH, (e) assembled zinc-air battery powering the commercial pink LED, (f) galvanostatic charge discharge curve of NiO/IrO$_2$-NF and Pt/C+IrO$_2$ air cathode based zinc-air batteries with 5 min charging and discharging at a constant current density of 2 mA cm^{-1}, (g) zinc-air battery powered overall water splitting assembly for sustainable hydrogen production, (h) assembled NiO/IrO$_2$-NF based air cathode displaying an open circuit voltage of 1.55 V.

phase segregation at higher working potentials due to intermittent reduction during the discharge cycle as displayed in Fig. 7c [63]. Also, the FE-SEM mapping and its corresponding EDS spectrum in Figure S32 shows the presence of metals in the structure at higher magnifications. Further, the overall EDAX mapping in Fig. 7d(i-iv) and individual elemental mapping of Ir, Ni, O, and Zn confirms the uniform distribution within the NiO/IrO$_2$-NF electrocatalyst. Thus, the durability effects were limited to the creation of few distortions in the porous structure of the electrocatalysts. Inclusion of Zn-based electrolyte along with alkaline KOH can potentially reduce the formation of dendrites and rapid dissolution of the anode during long term charge and discharge cycles

[64]. Hence, minimal deposition of zinc hydroxide was observed in the EDS spectrum, which is from the anodic zinc plate as shown in Fig. 7e. The survey spectrum in Fig. 7f shows the presence of Ir 4 f, Ni 2p, and O 1 s with only a slight change in their binding energy, indicating the outstanding retention efficiency of the optimal NiO/IrO$_2$-NF. The high resolution Ir 4 f in Fig. 7g indicates an increase in binding energy (61.68 eV to 61.88 eV), which is mainly due to the surface oxidation during the reaction. Also, the change in intensity and binding energy of Ir^{3+} and Ir^{4+} indicates their active involvement and extended oxide formation during the reaction [65]. High resolution Ni 2p spectra in Fig. 7h showed an increase in their binding energy (854.48 eV to
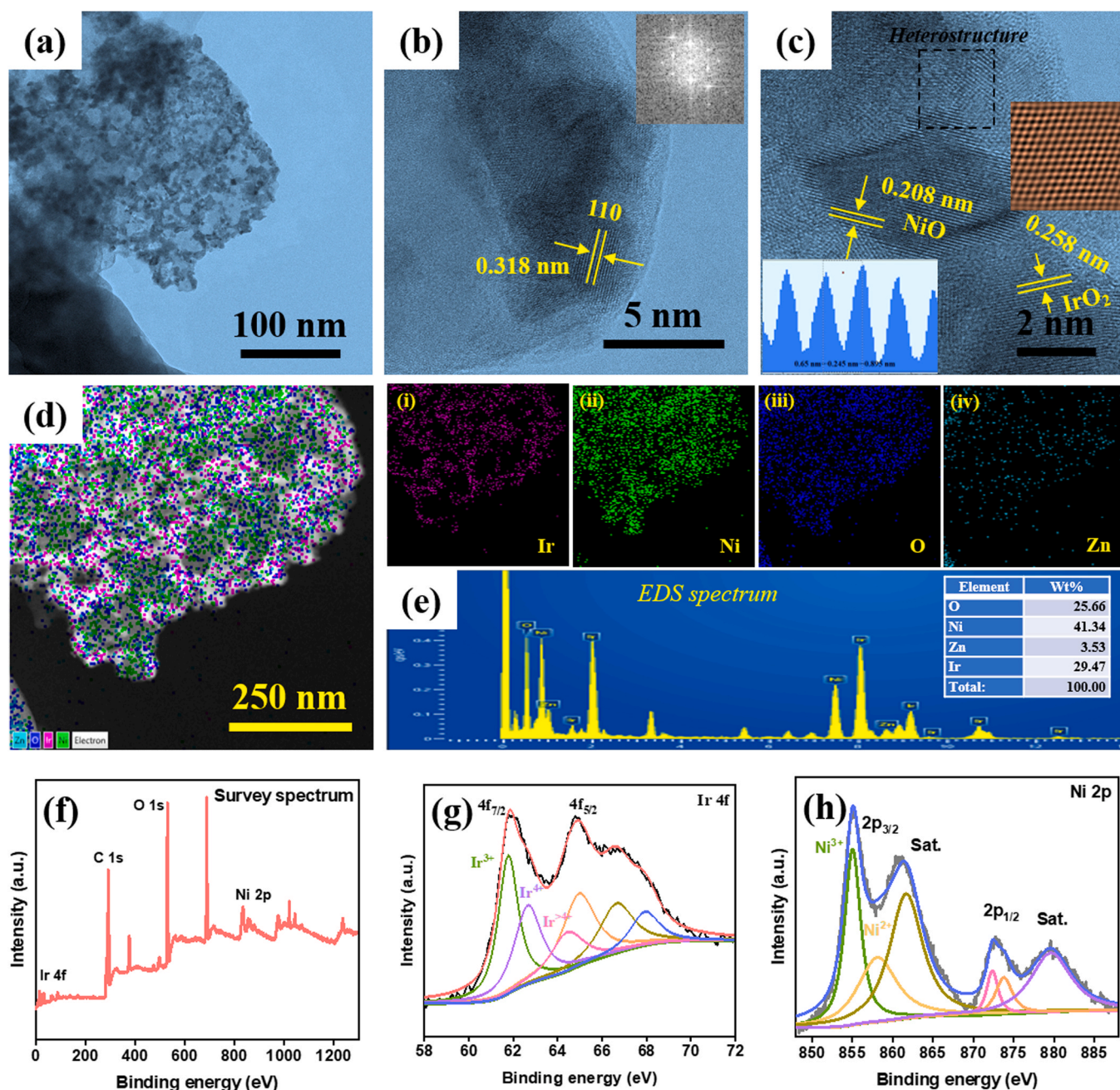
Fig. 7. Post morphological analysis of NiO/IrO$_2$-NF air cathode after 100 h charge discharge test in 6 M KOH + 0.2 M Zn (CH$_3$CO$_2$)$_2$ medium. (a-b) CS-TEM (inset: corresponding FFT pattern), (c) HR-TEM image (inset: lattice spacing and heterostructured region), (d) HAADF-STEM overall elemental mapping concerning (i) Ir, (ii) Ni, (iii) O, and (iv) Zn, (e) EDS map spectrum with elemental composition; Post stability XPS analysis of NiO/IrO$_2$-NF air cathode after 100 h charge discharge, (f) XPS survey spectrum, high resolution spectra of (g) Ir 4 f, (h) Ni 2p.

855.08 eV) and active involvement of the Ni^{3+} oxidation state. This increase in average oxidation state of Ni atoms in NiO/IrO$_2$-NF significantly enhanced the OER/ORR activity [66]. During the reaction, the NiO converted into Ni-OOH, and this reconfiguration may improve the catalytic activity by promoting the O* adsorption during long term stability measurements [67]. Such formation of metal oxide/hydroxide during the stability measurements might potentially exposes to more active sites on the catalytic surface [68]. This observed linear pattern indicates the equal involvement of a greater number of Ir and Ni active sites due to the crucial double phase coupling and mesoporous nature with exposed active sites of the electrocatalyst [69]. O 1 s spectra in Figure S33a indicates the retention of metal oxide interaction along with meta hydroxide formation on the catalytic surface due to intermittent

oxidation and reduction [70]. The increase in oxygen intensity after durability testing was due to O$_2$/H$_2$O adsorption, indicating the excellent O* adsorption on the surface [71]. Presence of Zn 2p spectra (Figure S33b) is due to the deposition of zinc hydroxide during the reaction from the Zn anode. These results clearly show that the optimal NiO/IrO$_2$-NF provides physical and electrochemical advantages over the commercial state of the art electrocatalysts, making it a potential candidate for future energy storage and conversion applications.

4. Conclusion

To summarize, we developed a rational strategy to prepare an efficient double phase mesoporous NiO/IrO$_2$-NF electrocatalyst using a

simple chemical blow approach with a subsequent calcination step. XRD, FE-SEM, TEM, HR-TEM, BET, XPS, and XAS analysis were used to characterize the formation of NiO/IrO_2-NF and investigate the hetero-structured and mesoporous nature of the prepared electrocatalysts. The results revealed that the NiO/IrO_2-NF exhibited a larger surface area and catalytic nature than its unitary components due to the double phase coupling strategy. Further, density functional theory calculations for HER, OER, and ORR mechanistic pathways assures the enhanced catalytic efficiency of the NiO/IrO_2-NF. The optimized NiO/IrO_2-NF displayed a significantly lower overpotentials and prolonged alkaline stability towards HER (η_{10}=42 mV) and OER (η_{10}=240 mV) at a constant current density of 10 mA cm^{-2}, outperforming state of the art electrocatalysts. Interestingly, the fabricated NiO/IrO_2-NF $\|$ NiO/IrO_2-NF electrolyzer reached a cell voltage of 1.51 V at a current density of 10 mA cm^{-2}, which was 0.04 V lower that commercial Pt/C $\|$ IrO_2. From a practical perspective, the water electrolyzer displayed an outstanding durability of 24 days (600 h) at a higher current density of 100 mA cm^{-2} with 96% potential retention, outperforming the advanced trifunctional electrocatalysts. Post stability HR-TEM and XPS investigations after 600 h prolonged durability revealed that the catalyst structure remained intact displaying the robustness and structural integrity. Finally, the fabricated NiO/IrO_2-NF air cathode based rechargeable zinc-air battery displayed an enhanced power density of 134.8 mW cm^{-2} and prolonged durability of 100/80/40 h at 2/5/10 mA cm^{-2}. This work provides a facile synthesis strategy for designing a highly mesoporous multi-phase electrocatalyst with maximum utilization of noble metal for futuristic clean and sustainable hydrogen production.

CRediT authorship contribution statement

S.C. Karthikeyan: Writing – review & editing, Writing – original draft, Investigation, Formal analysis, Data curation, Conceptualization. **Saleem Sidra:** Writing – original draft, Software, Investigation, Formal analysis, Data curation, Conceptualization. **Shanmugam Ramakrishnan:** Writing – review & editing, Validation, Investigation, Formal analysis, Data curation. **Do Hwan Kim:** Writing – review & editing, Software, Resources, Project administration, Funding acquisition, Formal analysis, Data curation. **Prince JJ Sagayaraj & Karthikeyan Sekar:** XAS spectra of standard NiO and Artemis fitting. **Dong Jin Yoo:** Writing – review & editing, Validation, Supervision, Resources, Project administration, Funding acquisition, Formal analysis, Data curation, Conceptualization.

Declaration of Competing Interest

The authors declare that they have no known competing financial interests or personal relationships that could have appeared to influence the work reported in this paper.

Data Availability

Data will be made available on request.

Acknowledgements

Appendix A. Supporting information

Supplementary data associated with this article can be found in the online version at doi:10.1016/j.apcatb.2024.124196.

References

[1] S. Chu, A. Majumdar, Opportunities and challenges for a sustainable energy future, Nature 488 (2012) 294–303, https://doi.org/10.1038/nature11475.

[2] D.M. Morales, M.A. Kazakova, S. Dieckhöfer, A.G. Selyutin, G.V. Golubtsov, W. Schuhmann, J. Masa, Trimetallic Mn-Fe-Ni oxide nanoparticles supported on multi-walled carbon nanotubes as high-performance bifunctional ORR/OER electrocatalyst in alkaline media, Adv. Funct. Mater. 30 (2020), https://doi.org/10.1002/adfm.201905992.

[3] H.B. Gray, Powering the planet with solar fuel, Nat. Chem. 1 (2009) 7, https://doi.org/10.1038/nchem.141.

[4] Z.W. Gao, J.Y. Liu, X.M. Chen, X.L. Zheng, J. Mao, H. Liu, T. Ma, L. Li, W.C. Wang, X.W. Du, Engineering NiO/NiFe LDH intersection to bypass scaling relationship for oxygen evolution reaction via dynamic tridimensional adsorption of intermediates, Adv. Mater. 31 (2019) 1–8, https://doi.org/10.1002/adma.201804769.

[5] N. Logeshwaran, S. Ramakrishnan, S.S. Chandrasekaran, M. Vinothkannan, A. R. Kim, S. Sengodan, D.B. Velusamy, P. Varadhan, J.H. He, D.J. Yoo, An efficient and durable trifunctional electrocatalyst for zinc–air batteries driven overall water splitting, Appl. Catal. B Environ. 297 (2021) 120405, https://doi.org/10.1016/j.apcatb.2021.120405.

[6] G. Zhou, G. Liu, X. Liu, Q. Yu, H. Mao, Z. Xiao, L. Wang, 1D/3D Heterogeneous assembling body as trifunctional electrocatalysts enabling zinc–air battery and self-powered overall water splitting, Adv. Funct. Mater. 32 (2022), https://doi.org/10.1002/adfm.202107608.

[7] Q. Dang, Y. Sun, X. Wang, W. Zhu, Y. Chen, F. Liao, H. Huang, M. Shao, Environmental carbon dots-Pt modified polyaniline nanosheet grown on carbon cloth as stable and high-efficient electrocatalyst for hydrogen evolution in pH-universal electrolyte, Appl. Catal. B Environ. 257 (2019) 117905, https://doi.org/10.1016/j.apcatb.2019.117905.

[8] L. Zu, X. Qian, S. Zhao, Q. Liang, Y.E. Chen, M. Liu, B.J. Su, K.H. Wu, L. Qu, L. Duan, H. Zhan, J.Y. Zhang, C. Li, W. Li, J.Y. Juang, J. Zhu, D. Li, A. Yu, D. Zhao, Self-assembly of Ir-based nanosheets with ordered interlayer space for enhanced electrocatalytic water oxidation, J. Am. Chem. Soc. 144 (2022) 2208–2217, https://doi.org/10.1021/jacs.1c11241.

[9] S. Ye, S. Xie, Y. Lei, X. Yang, J. Hu, L. Zheng, Z. Chen, Y. Fu, X. Ren, Y. Li, X. Ouyang, Q. Zhang, J. Liu, X. Sun, Modulating the electronic spin state by constructing dual-metal atomic pairs for activating the dynamic site of oxygen reduction reaction, Nano Res 16 (2023) 1869–1877, https://doi.org/10.1007/s12274-022-4979-x.

[10] S. Ye, Y. Lei, T. Xu, L. Zheng, Z. Chen, X. Yang, X. Ren, Y. Li, Q. Zhang, J. Liu, Deeply self-reconstructing CoFe(H$_3$O)(PO$_4$)$_2$ to low-crystalline Fe$_{0.5}$Co$_{0.5}$OOH with Fe^{3+}–O–Fe^{3+} motifs for oxygen evolution reaction, Appl. Catal. B Environ. 304 (2022) 120986, https://doi.org/10.1016/j.apcatb.2021.120986.

[11] S. Ye, Y. Zhang, W. Xiong, T. Xu, P. Liao, P. Zhang, X. Ren, C. He, L. Zheng, X. Ouyang, Q. Zhang, J. Liu, Construction of tetrahedral CoO$_4$vacancies for activating the high oxygen evolution activity of Co$_{3-x}$O$_4$-d porous nanosheet arrays, Nanoscale 12 (2020) 11079–11087, https://doi.org/10.1039/d0nr00744g.

[12] H. Zhang, T. Wang, A. Sumboja, W. Zang, J. Xie, D. Gao, S.J. Pennycook, Z. Liu, C. Guan, J. Wang, Integrated hierarchical carbon flake arrays with hollow P-doped CoSe$_2$ nanoclusters as an advanced bifunctional catalyst for Zn–air batteries, Adv. Funct. Mater. 28 (2018), https://doi.org/10.1002/adfm.201804846.

[13] R. Santhosh Kumar, S.C. Karthikeyan, S. Ramakrishnan, S. Vijayapradeep, A. Rhan Kim, J.S. Kim, D. Jin Yoo, Anion dependency of spinel type cobalt catalysts for efficient overall water splitting in an acid medium, Chem. Eng. J. 451 (2023) 138471, https://doi.org/10.1016/j.cej.2022.138471.

[14] S.C. Karthikeyan, S. Prabhakaran, R.S. Kumar, S. Ramakrishnan, A.R. Kim, D. H. Kim, D.J. Yoo, High-efficiency sustainable energy driven alkaline/seawater electrolysis using a novel hetero-structured non-noble bimetal telluride nanorods, Mater. Today Nano 24 (2023) 100412, https://doi.org/10.1016/j.mtnano.2023.100412.

[15] D. Ren, J. Ying, M. Xiao, Y.P. Deng, J. Ou, J. Zhu, G. Liu, Y. Pei, S. Li, A.M. Jauhar, H. Jin, S. Wang, D. Su, A. Yu, Z. Chen, Hierarchically porous multimetal-based carbon nanorod hybrid as an efficient oxygen catalyst for rechargeable zinc–air batteries, Adv. Funct. Mater. 30 (2020), https://doi.org/10.1002/adfm.201908167.

[16] S. Jin, Are metal chalcogenides, nitrides, and phosphides oxygen evolution catalysts or bifunctional catalysts? ACS Energy Lett. 2 (2017) 1937–1938, https://doi.org/10.1021/acsenergylett.7b00679.

[17] C. Zhou, X. Chen, S. Liu, Y. Han, H. Meng, Q. Jiang, S. Zhao, F. Wei, J. Sun, T. Tan, R. Zhang, Superdurable bifunctional oxygen electrocatalyst for high-performance zinc-air batteries, J. Am. Chem. Soc. 144 (2022) 2694–2704, https://doi.org/10.1021/jacs.1c11675.

[18] A. Kulkarni, S. Siahrostami, A. Patel, J.K. Nørskov, Understanding catalytic activity trends in the oxygen reduction reaction, Chem. Rev. 118 (2018) 2302–2312, https://doi.org/10.1021/acs.chemrev.7b00488.

[19] T. Li, W. Zeng, Z. Wang, Quasi-one-dimensional metal-oxide-based heterostructural gas-sensing materials: a review, Sens. Actuators, B Chem. 221 (2015) 1570–1585, https://doi.org/10.1016/j.snb.2015.08.003.

[20] J. Su, G. Xia, R. Li, Y. Yang, J. Chen, R. Shi, P. Jiang, Q. Chen, Co$_3$ZnC/Co nano heterojunctions encapsulated in N-doped graphene layers derived from PBAs as highly efficient bi-functional OER and ORR electrocatalysts, J. Mater. Chem. A. 4 (2016) 9204–9212, https://doi.org/10.1039/c6ta00945j.

[21] M. Steimecke, G. Seiffarth, C. Schneemann, F. Oehler, S. Förster, M. Bron, Higher-valent nickel oxides with improved oxygen evolution activity and stability in alkaline media prepared by high-temperature treatment of Ni(OH)$_2$, ACS Catal. 10 (2020) 3595–3603, https://doi.org/10.1021/acscatal.9b04788.

[22] V. Bisogni, S. Catalano, R.J. Green, M. Gibert, R. Scherwitzl, Y. Huang, V. N. Strocov, P. Zubko, S. Balandeh, J.M. Triscone, G. Sawatzky, T. Schmitt, Ground-state oxygen holes and the metal-insulator transition in the negative charge-transfer rare-earth nickelates, Nat. Commun. 7 (1) (2016) 8, https://doi.org/10.1038/ncomms13017.

[23] Q. Wang, X. Huang, Z.L. Zhao, M. Wang, B. Xiang, J. Li, Z. Feng, H. Xu, M. Gu, Ultrahigh-loading of Ir single atoms on NiO matrix to dramatically enhance oxygen evolution reaction, J. Am. Chem. Soc. 142 (2020) 7425–7433, https://doi.org/10.1021/jacs.9b12642.

[24] Q. Li, S. Dong, H. Xie, J. Ren, X. Hu, Y. Li, H. Zhao, Z. Liu, F. Sun, Controllable synthesis of crystal-amorphous heterostructures in transition metal phosphide and enhancement mechanism for overall water splitting, Appl. Surf. Sci. 647 (2024) 158961, https://doi.org/10.1016/j.apsusc.2023.158961.

[25] H.N. Nong, L. Gan, E. Willinger, D. Teschner, P. Strasser, IrOx core-shell nanocatalysts for cost- and energy-efficient electrochemical water splitting, Chem. Sci. 5 (2014) 2955–2963, https://doi.org/10.1039/c4sc01065e.

[26] H.N. Nong, H.S. Oh, T. Reier, E. Willinger, M.G. Willinger, V. Petkov, D. Teschner, P. Strasser, Oxide-supported IrNiOx core-shell particles as efficient, cost-effective, and stable catalysts for electrochemical water splitting, Angew. Chem. - Int. Ed. 54 (2015) 2975–2979, https://doi.org/10.1002/anie.201411072.

[27] A.L. Patterson, The scherrer formula for X-ray particle size determination, Phys. Rev. 56 (1939) 978–982, https://doi.org/10.1103/PhysRev.56.978.

[28] Z. Shi, Y. Wang, J. Li, X. Wang, Y. Wang, Y. Li, W. Xu, Z. Jiang, C. Liu, W. Xing, J. Ge, Confined Ir single sites with triggered lattice oxygen redox: toward boosted and sustained water oxidation catalysis, Joule 5 (2021) 2164–2176, https://doi.org/10.1016/j.joule.2021.05.018.

[29] L. Yang, L. Shi, H. Chen, X. Liang, B. Tian, K. Zhang, Y. Zou, X. Zou, A highly active, long-lived oxygen evolution electrocatalyst derived from open-framework iridates, Adv. Mater. 35 (2023) 1–9, https://doi.org/10.1002/adma.202208539.

[30] H. Lee, J.Y. Kim, S.Y. Lee, J.A. Hong, N. Kim, J. Baik, Y.J. Hwang, Comparative study of catalytic activities among transition metal-doped nanoparticles, Sci. Rep. 8 (2018) 2–9, https://doi.org/10.1038/s41598-018-35116-w.

[31] W. Sun, L.M. Cao, J. Yang, Conversion of inert cryptomelane-type manganese oxide into a highly efficient oxygen evolution catalyst via limited Ir doping, J. Mater. Chem. A 4 (2016) 12561–12570, https://doi.org/10.1039/c6ta03011d.

[32] S.K. Oh, H.W. Kim, Y.K. Kwon, M.J. Kim, E.A. Cho, H.S. Kwon, Porous Co-P foam as an efficient bifunctional electrocatalyst for hydrogen and oxygen evolution reactions, J. Mater. Chem. A. 4 (2016) 18272–18277, https://doi.org/10.1039/C6TA06761A.

[33] C. Bae, T.A. Ho, H. Kim, S. Lee, S. Lim, M. Kim, H. Yoo, J.M. Montero-Moreno, J. H. Park, H. Shin, Bulk layered heterojunction as an efficient electrocatalyst for hydrogen evolution, Sci. Adv. 3 (2017), https://doi.org/10.1126/sciadv.1602215.

[34] R. Zhang, G. Wang, Z. Wei, X. Teng, J. Wang, J. Miao, Y. Wang, F. Yang, X. Zhu, C. Chen, E. Zhou, W. Hu, X. Sun, A Fe-Ni5P4/Fe-Ni2P heterojunction electrocatalyst for highly efficient solar-to-hydrogen generation, J. Mater. Chem. A. 9 (2021) 1221–1229, https://doi.org/10.1039/d0ta08631b.

[35] K. Harish, J. Balamurugan, T.T. Nguyen, N.H. Kim, J.H. Lee, Advanced interfacial engineering of oxygen-enriched FexSn1−xOSe nanostructures for efficient overall water splitting and flexible zinc-air batteries, Appl. Catal. B Environ. 305 (2022) 120924, https://doi.org/10.1016/j.apcatb.2021.120924.

[36] X. Xu, Y. Chen, W. Zhou, Z. Zhu, C. Su, M. Liu, A Perovskite Electrocatalyst for Efficient Hydrogen Evolution Reaction, COMMUNICATION (2016) 6442–6448, https://doi.org/10.1002/adma.201600005.

[37] G. Zhao, P. Li, N. Cheng, S.X. Dou, W. Sun, An Ir/Ni(OH)2 heterostructured electrocatalyst for the oxygen evolution reaction: breaking the scaling relation, stabilizing iridium(V), and beyond, Adv. Mater. 32 (2020) 1–9, https://doi.org/10.1002/adma.202000872.

[38] T. Reier, Z. Pawolek, S. Cherevko, M. Bruns, T. Jones, D. Teschner, S. Selve, A. Bergmann, H.N. Nong, R. Schlögl, K.J.J. Mayrhofer, P. Strasser, Molecular insight in structure and activity of highly efficient, low-Ir Ni-oxide catalysts for electrochemical water splitting (OER), J. Am. Chem. Soc. 137 (2015) 13031–13040, https://doi.org/10.1021/jacs.5b07788.

[39] G. Buvat, M.J. Eslamibidgoli, A.H. Youssef, S. Garbarino, A. Ruediger, M. Eikerling, D. Guay, Effect of XIe6 octahedron distortion on the OER activity at (100) IrO2 thin film, ACS Catal. 10 (2020) 806–817, https://doi.org/10.1021/acscatal.9b04347.

[40] J. Qian, X. Guo, T. Wang, P. Liu, H. Zhang, D. Gao, Applied Catalysis B: environmental Bifunctional porous Co-doped NiO nano flowers electrocatalysts for rechargeable zinc-air batteries, Appl. Catal. B Environ. 250 (2019) 71–77, https://doi.org/10.1016/j.apcatb.2019.03.021.

[41] M. Yu, G. Moon, E. Bill, Optimizing Ni − Fe oxide electrocatalysts for oxygen evolution reaction by using hard templating as a toolbox (2019). https://doi.org/10.1021/acsaem.8b01769.

[42] D.Y. Kuo, J.K. Kawasaki, J.N. Nelson, J. Kloppenburg, G. Hautier, K.M. Shen, D. G. Schlom, J. Suntivich, Influence of surface adsorption on the oxygen evolution reaction on IrO2 (110), J. Am. Chem. Soc. 139 (2017) 3473–3479, https://doi.org/10.1021/jacs.6b11932.

[43] Y. Hao, X. Cao, C. Lei, Z. Chen, X. Yang, M. Gong, Chemical oxygen species on electrocatalytic materials during oxygen evolution reaction, Mater. Today Catal. 2 (2023) 100012, https://doi.org/10.1016/j.mtcata.2023.100012.

[44] Q.T. Trinh, K. Bhola, P.N. Amaniampong, F. Jérôme, S.H. Mushrif, Synergistic Application of XPS and DFT to investigate metal oxide surface catalysis, J. Phys. Chem. C. 122 (2018) 22397–22406, https://doi.org/10.1021/acs.jpcc.8b05499.

[45] A. Minguzzi, C. Locatelli, O. Lugaresi, E. Achilli, G. Cappelletti, M. Scavini, M. Coduri, P. Masala, B. Sacchi, A. Vertova, P. Ghigna, S. Rondinini, Easy accommodation of different oxidation states in iridium oxide nanoparticles with different hydration degree as water oxidation electrocatalysts, ACS Catal. 5 (2015) 5104–5115, https://doi.org/10.1021/acscatal.5b01281.

[46] D.F. Abbott, D. Lebedev, K. Waltar, M. Povia, M. Nachtegaal, E. Fabbri, C. Copéret, T.J. Schmidt, Iridium oxide for the oxygen evolution reaction: correlation between particle size, morphology, and the surface hydroxo layer from operando XAS, Chem. Mater. 28 (2016) 6591–6604, https://doi.org/10.1021/acs.chemmater.6b02625.

[47] J. Shan, C. Guo, Y. Zhu, S. Chen, L. Song, M. Jaroniec, Y. Zheng, S.Z. Qiao, Charge-redistribution-enhanced nanocrystalline Ru@IrOx electrocatalysts for oxygen evolution in acidic media, Chem 5 (2019) 445–459, https://doi.org/10.1016/j.chempr.2018.11.010.

[48] S. Czioska, A. Boubnov, D. Escalera-López, J. Geppert, A. Zagalskaya, P. Röse, E. Saraçi, V. Alexandrov, U. Krewer, S. Cherevko, J.D. Grunwaldt, Increased Ir-Ir interaction in iridium oxide during the oxygen evolution reaction at high potentials probed by operando spectroscopy, ACS Catal. 11 (2021) 10043–10057, https://doi.org/10.1021/acscatal.1c02074.

[49] W. Sun, Z. Wang, Z. Zhou, Y. Wu, W.Q. Zaman, M. Tariq, L.M. Cao, X.Q. Gong, J. Yang, A promising engineering strategy for water electro-oxidation iridate catalysts: Via coordination distortion, Chem. Commun. 55 (2019) 5801–5804, https://doi.org/10.1039/c9cc02447f.

[50] H.N. Nong, T. Reier, H.-S. Oh, M. Gliech, P. Paciok, T.H.T. Vu, D. Teschner, M. Heggen, V. Petkov, R. Schlögl, T. Jones, P. Strasser, A unique oxygen ligand environment facilitates water oxidation in hole-doped IrNiOx core–shell electrocatalysts, Nat. Catal. 1 (2018) 841–851, https://doi.org/10.1038/s41929-018-0153-y.

[51] A. Minguzzi, O. Lugaresi, E. Achilli, C. Locatelli, A. Vertova, P. Ghigna, S. Rondinini, Observing the oxidation state turnover in heterogeneous iridium-based water oxidation catalysts, Chem. Sci. 5 (2014) 3591–3597, https://doi.org/10.1039/c4sc00975d.

[52] Y. Lei, T. Xu, S. Ye, L. Zheng, P. Liao, W. Xiong, J. Hu, Y. Wang, J. Wang, X. Ren, C. He, Q. Zhang, J. Liu, X. Sun, Engineering defect-rich Fe-doped NiO coupled Ni cluster nanotube arrays with excellent oxygen evolution activity, Appl. Catal. B Environ. 285 (2021) 119809, https://doi.org/10.1016/j.apcatb.2020.119809.

[53] S. Siracusano, V. Baglio, S.A. Grigoriev, L. Merlo, V.N. Fateev, A.S. Aricò, The influence of iridium chemical oxidation state on the performance and durability of oxygen evolution catalysts in PEM electrolysis, J. Power Sources 366 (2017) 105–114, https://doi.org/10.1016/j.jpowsour.2017.09.020.

[54] R. Lontio Fomekong, J. Regner, S. Akir, F.M. Oliveira, J. Luxa, A.V. Papavasileiou, J. Boitumelo, L. Dekanovsky, Z. Sofer, Enhancing the electrocatalytic properties of a one-pot synthesis of defect-rich 2D/2D nanoheterointerface of titanium carbo-oxide and molybdenum disulfide for hydrogen evolution reaction in acidic medium, ACS Sustain. Chem. Eng. 11 (2023) 14528–14537, https://doi.org/10.1021/acssuschemeng.3c03621.

[55] X. Gu, Z. Liu, M. Li, J. Tian, L. Feng, Surface structure regulation and evaluation of FeNi-based nanoparticles for oxygen evolution reaction, Appl. Catal. B Environ. 297 (2021) 120462, https://doi.org/10.1016/j.apcatb.2021.120462.

[56] M. Kuang, Q. Wang, H. Ge, P. Han, Z. Gu, A.M. Al-Enizi, G. Zheng, CuCoOx/FeOOH core-shell nanowires as an efficient bifunctional oxygen evolution and reduction catalyst, ACS Energy Lett. 2 (2017) 2498–2505, https://doi.org/10.1021/acsenergylett.7b00835.

[57] Y. Liang, Y. Li, H. Wang, J. Zhou, J. Wang, T. Regier, H. Dai, Co3O4 nanocrystals on graphene as a synergistic catalyst for oxygen reduction reaction, Nat. Mater. 10 (2011) 780–786, https://doi.org/10.1038/nmat3087.

[58] I. Spanos, J. Masa, A. Zeradjanin, R. Schlögl, The Effect of iron impurities on transition metal catalysts for the oxygen evolution reaction in alkaline environment: activity mediators or active sites? Catal. Lett. 151 (2021) 1843–1856, https://doi.org/10.1007/s10562-020-03478-4.

[59] J. Zhang, J. Zhang, F. He, Y. Chen, J. Zhu, D. Wang, S. Mu, H.Y. Yang, Defect and doping co-engineered non-metal nanocarbon ORR electrocatalyst, Nano-Micro Lett. 13 (1) (2021) 30, https://doi.org/10.1007/s40820-020-00579-y.

[60] J. Wang, D.T. Tran, K. Chang, S. Prabhakaran, J. Zhao, D.H. Kim, N.H. Kim, J. H. Lee, Hierarchical Ni@CNTs-bridged MoxC/Ni2P heterostructure micro-pillars for enhanced seawater splitting and Mg/seawater battery, Nano Energy 111 (2023) 108440, https://doi.org/10.1016/j.nanoen.2023.108440.

[61] K. Chang, D.T. Tran, J. Wang, K. Dong, S. Prabhakaran, D.H. Kim, N.H. Kim, J. H. Lee, Triphasic Ni2P−Fe2P−CoP heterostructure interfaces for efficient overall water splitting powered by solar energy, Appl. Catal. B Environ. 338 (2023) 123016, https://doi.org/10.1016/j.apcatb.2023.123016.

[62] N.S. Gultom, T.S. Chen, M.Z. Silitonga, D.H. Kuo, Overall water splitting realized by overall sputtering thin-film technology for a bifunctional MoNiFe electrode: a green technology for green hydrogen, Appl. Catal. B Environ. 322 (2023) 122103, https://doi.org/10.1016/j.apcatb.2022.122103.

[63] F.Y. Chen, Z.Y. Wu, Z. Adler, H. Wang, Stability challenges of electrocatalytic oxygen evolution reaction: From mechanistic understanding to reactor design, Joule 5 (2021) 1704–1731, https://doi.org/10.1016/j.joule.2021.05.005.

[64] D. Deckenbach, J.J. Schneider, A Long-overlooked pitfall in rechargeable zinc–air batteries: proper electrode balancing, Adv. Mater. Interfaces 10 (2023), https://doi.org/10.1002/admi.202202494.

[65] S.C. Karthikeyan, R. Santhosh Kumar, S. Ramakrishnan, S. Prabhakaran, A.R. Kim, D.H. Kim, D.J. Yoo, Efficient alkaline water/seawater electrolysis by development of ultra-low IrO2 nanoparticles decorated on hierarchical MnO2/rGO nanostructure, ACS Sustain. Chem. Eng. (2022), https://doi.org/10.1021/acssuschemeng.2c04074.

[66] B.J. Kim, E. Fabbri, D.F. Abbott, X. Cheng, A.H. Clark, M. Nachtegaal, M. Borlaf, I. E. Castelli, T. Graule, T.J. Schmidt, Functional role of Fe-doping in Co-based

perovskite oxide catalysts for oxygen evolution reaction, J. Am. Chem. Soc. 141 (2019) 5231–5240, https://doi.org/10.1021/jacs.8b12101.

[67] S. Bi, Z. Geng, Y. Wang, Z. Gao, L. Jin, M. Xue, C. Zhang, Multi-stage porous Nickel–Iron Oxide electrode for high current alkaline water electrolysis, Adv. Funct. Mater. (2023), https://doi.org/10.1002/adfm.202214792.

[68] L. Wu, J. Li, C. Shi, Y. Li, H. Mi, L. Deng, Q. Zhang, C. He, X. Ren, Rational design of the FeS_2/NiS_2 heterojunction interface structure to enhance the oxygen electrocatalytic performance for zinc-air batteries, J. Mater. Chem. A. 10 (2022) 16627–16638, https://doi.org/10.1039/d2ta03554e.

[69] Y. Luo, M. Wen, J. Zhou, Q. Wu, G. Wei, Y. Fu, Highly-exposed Co-CoO derived from nanosized ZIF-67 on N-doped porous carbon foam as efficient electrocatalyst for zinc-air battery, Small 2302925 (2023) 1–9, https://doi.org/10.1002/smll.202302925.

[70] X. Liu, J. Meng, J. Zhu, M. Huang, B. Wen, R. Guo, L. Mai, Comprehensive understandings into complete reconstruction of precatalysts: synthesis, applications, and characterizations, Adv. Mater. 33 (2021) 1–34, https://doi.org/10.1002/adma.202007344.

[71] F. Qiang, J. Feng, H. Wang, J. Yu, J. Shi, M. Huang, Z. Shi, S. Liu, P. Li, L. Dong, Oxygen engineering enables N-doped porous carbon nanofibers as oxygen reduction/evolution reaction electrocatalysts for flexible zinc-air batteries, ACS Catal. 12 (2022) 4002–4015, https://doi.org/10.1021/acscatal.2c00164.